Characterization of active material from lithium-ion batteries by XRD and SEM

Sabrina Sasse

Angaben zur Veröffentlichung / Publication details:

Sasse, Sabrina. 2024. “Characterization of active material from lithium-ion batteries by XRD and SEM.” Augsburg: Universität Augsburg.

Universität Augsburg
Mathematisch-Naturwissenschaftlich-Technische Fakultät

Characterization of Active Material from Lithium-Ion Batteries by XRD and SEM

Bachelor Thesis in Industrial Engineering at the Faculty of Mathematics, Natural Science, and Materials Engineering at the University of Augsburg

Written by: Sabrina Sasse (Matr.-Nr: 2049377)

Submitted at: 07.08.2024

Written at: Institute of Material Resource Management

First reviewer: Prof. Dr. Daniel Vollprecht

Second reviewer: Prof. Dr.-Ing. Jan Paul Linder

Abstract

This bachelor thesis investigates the characterization of active material from spent lithium-ion batteries (SLIBs) using X-ray diffraction (XRD) and scanning electron microscopy coupled with energy dispersive X-ray spectroscopy (SEM-EDS). With the growing use of lithium-ion batteries (LIBs) in electric vehicles (EVs) and other applications, the proper recycling of these batteries is crucial to mitigate environmental hazards and recover valuable materials. This study aims to address three primary research questions: (1) the extent to which SLIB active material can be characterized using XRD and SEM-EDS, (2) the improvement in XRD characterization of active material through simulated froth flotation, and (3) the fundamental efficiency of simulated froth flotation in separating Graphite and Lithium metal oxide (LMOs).

The research begins with a comprehensive theoretical background, covering the structure and composition of LIBs, and current recycling processes, including mechanical pretreatment and metallurgical methods. The materials analyzed in this study were sourced from EV-SLIBs with NMC and Graphite as the primary cathode and anode materials, respectively. Initial XRD analysis revealed multiple mineralogical phases, thus requiring the use of SEM-EDS to provide detailed elemental composition data. The SEM-EDS results indicated the presence of key elements such as Al, C, Co, Cu, Mn, Ni, O, and Si consistent with typical LIB compositions. Notably, the high oxygen content suggested prior thermal treatment. XRD analysis further identified the presence of Graphite, CoO, MnO, various Li compounds, and metallic Ni, with some discrepancies in elemental proportions between XRD and SEM-EDS results. To enhance XRD characterization, a simulated froth flotation process was employed, which successfully reduced the number of mineralogical phases and provided clearer diffraction patterns. The froth flotation process demonstrated effective separation of Graphite and LMOs, improving the clarity of XRD analysis. The froth product showed an increased concentration of Graphite and a decreased concentration of Ni, while the pulp product contained higher proportions of $Li_2(CO_3)$. These findings support the viability of froth flotation as a pretreatment step in LIB recycling, enhancing the recovery of valuable materials and contributing to a more sustainable recycling process.

In conclusion, this thesis provides a detailed characterization of SLIB active materials using XRD and SEM-EDS, highlights the benefits of froth flotation in improving XRD analysis, and underscores the importance of developing efficient recycling methods to support the circular economy in LIB production and disposal.

Table of Contents

List of Figures

List of Tables

List of Abbreviations

EU	European Union
EV	Electrical vehicle
FoM	Figure of merit
GHG	Greenhouse gas
LIB	Lithium-ion battery
LMO	Lithium metal oxide
NMC	Nickel-Manganese-Cobalt
PVDF	Polyvinylidene fluoride
RQ	Research question
SEM-EDS	Scanning electron microscopy coupled with energy dispersive X-ray spectroscopy
SLIB	Spent lithium-ion battery
XRD	X-ray diffraction

1 Introduction

Advancements in mobility have made the transport sector the second-largest contributor to global greenhouse gas (GHG) emissions (Eva et al.; Ritchie et al., 2024). Consequently, rising GHG emissions and its effects on climate change have prompted the European Union (EU) to ban the sale of petrol and diesel cars by 2035, allowing only carbon emission-free vehicles (European Parliament, 2023). In 2022, there were over 26 million electrical vehicles (EVs) on the road, a 60 % increase from 2021 (IEA, 2024). Lithium-ion batteries (LIBs) are to date the most popular choice for EVs, with demand expected to increase 14-fold by 2030, mainly due to an increase in EV production (European Parliament, 2022; Xie & Lu, 2020). The rapid growth of LIB production is also due to their versatility in sustainable energy systems and portable electronic devices (Kim et al., 2020; Ruismäki et al., 2020). Accordingly, LIB waste is anticipated to rise to 8 million tons by 2040 (Stone, 2021).

Improper disposal of spent LIBs (SLIBs) can lead to toxic electrolytes and heavy metals contaminating the groundwater and harmful fuels from burning batteries being released into the atmosphere (Bhar et al., 2023; Rey et al., 2021). Raw materials used in LIBs, such as Lithium (Li), Cobalt (Co), Nickel (Ni), Manganese (Mn), and natural Graphite, are predominantly mined, refined and manufactured in countries like Chile, Congo, and China (Baum et al., 2022; DERA, 2021; Sun et al., 2019). This uneven distribution has led to supply risks and caused ecological and sociological issues, for example water mismanagement in Chile and child labor in Congo, due to the mass extraction of the required raw materials (Brückner et al., 2020; DERA, 2021; Windisch-Kern et al., 2022). For these reasons, the EU has categorized Co, Li, Mn, Ni, and natural Graphite as critical and strategic critical raw materials by 2023 (European Commission & Directorate General for Internal Market, Industry, Entrepreneurship and SMEs., 2023). Therefore, improving current LIB waste management and increasing recycling efforts are essential to support sustainable usage and prevent detrimental environmental effects from improper storage and disposal of SLIBs (Baum et al., 2022; Lai et al., 2022; Z. Yang et al., 2022).

Graphite, the most commonly used anode material in Nickel-Manganese-Cobalt (NMC) based LIBs, represents 15 – 20 % of a LIB's weight, similar to the cathode (Baum et al., 2022; Rey et al., 2021; Thompson et al., 2020). However, the anode's economic value accounts for only 10 % of the total battery value, while the cathode makes up 60 % (Rey et al., 2021; Thompson et al., 2020). This discrepancy leads to insufficient Graphite recovery during LIB recycling, as efforts are focused on the more valuable cathode materials and metals in LIBs (Rey et al., 2021; Thompson et al., 2020). Pyro- and

hydrometallurgy, two conventional metallurgical recycling methods, are commonly practiced in the LIB recycling industry and reflect the uneven recycling efforts (Chernyaev et al., 2024; Vanderbruggen et al., 2021). Pyrometallurgy uses Graphite as a reduction agent and heat to produce mixed metal alloys of Co, Copper (Cu), and Ni, and slag containing Aluminum (Al) and Li, while hydrometallurgy uses solvents to leach and separate valuable metals (Baum et al., 2022; Rey et al., 2021). Consequently, these methods mainly recover cathode materials, often leaving Graphite unrecovered (Chernyaev et al., 2024; Vanderbruggen et al., 2021). With the expected rise in LIB waste, developing environmentally friendly recycling methods for Graphite is crucial to support a circular economy and ensure a sustainable future for LIBs and EVs (Rey et al., 2021; Stone, 2021; Velázquez-Martínez et al., 2019).

Before applying metallurgical methods to recover battery-grade materials, SLIBs are typically pretreated by discharging, shredding, and sorting (Windisch-Kern et al., 2022). This process produces a homogenous black mass, otherwise known as active material, consisting mainly of fine electrode materials, with impurities such as Cu, Al, organic electrolytes, and binder materials (Vanderbruggen et al., 2021; Windisch-Kern et al., 2022). Froth flotation, which relies on the hydrophobic and hydrophilic differences between materials, has proven to be an effective pretreatment option to separate Graphite and lithium-metal-oxides (LMOs) (Vanderbruggen et al., 2021; Yu et al., 2023). This method uses surface-active reagents, air bubbles, and agitation to separate materials into froth and pulp products and is particularly suitable for the fine particle separation (Bhar et al., 2023; Ma et al., 2023; Pawlik, 2022). The separation process allows both Graphite and LMOs to be recovered and processed into battery-grade material through subsequent refinement processes, like hydrometallurgical methods (Brückner et al., 2020; Vanderbruggen et al., 2021).

This bachelor thesis aims to analyze the material composition of SLIB active material with Graphite and NMC-based electrode materials. This study addresses the following research questions (RQ):

1. To what extent can the active material from SLIBs be characterized using X-ray diffraction (XRD) and scanning electron microscopy with coupled energy dispersive X-ray spectroscopy (SEM-EDS)?
2. To what extent does a simulated froth flotation process improve the XRD characterization of the active material by reducing the number of mineralogical phases present in the active material?
3. To what extent can the simulated froth flotation be applied in this study to fundamentally investigate the separation efficiency of Graphite and LMOs?

2 Theoretical Background

This chapter intends to present a comprehensive overview of topics relevant for a more profound understanding of the material composition of active material from SLIBs. The first subchapter, 2.1, focuses on the structural and material composition of EV-LIBs, which is followed by the second subchapter, 2.2, dealing with the recycling of SLIBs. This subchapter is divided into 2.2.1, mechanical pretreatment steps and 2.2.2, metallurgical recycling processes of LIBs.

2.1 Overview of Lithium-Ion Batteries

LIBs have greatly influenced the development of passenger car engines and have become the preferred choice for EVs (Thielmann et al., 2020; Xie & Lu, 2020). They are commonly organized into packs consisting of a collection of battery modules, and its housing components, including the exterior casing, a cooling system, and a battery management system (DERA, 2021; Yu et al., 2023). Each module contains a series of cells, available in cylindrical, pouch, and prismatic forms, with prismatic cells most common in EVs due to their high energy capacity (Brückner et al., 2020; Thompson et al., 2020; Wen et al., 2020). For a better understanding, an overview of the LIB structure is visualized in Figure 1. Variations in manufacturing processes among automotive brands, however, complicate recycling due to differences in battery structure and material content, making sorting and disassembly challenging (Bhar et al., 2023; Windisch-Kern et al., 2022; Yu et al., 2023).

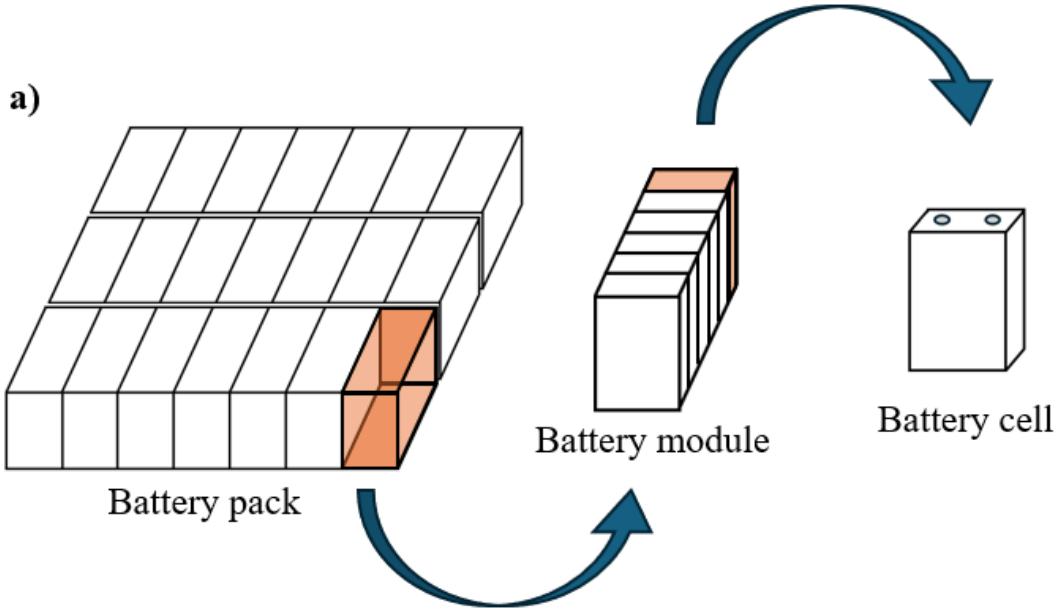

continued

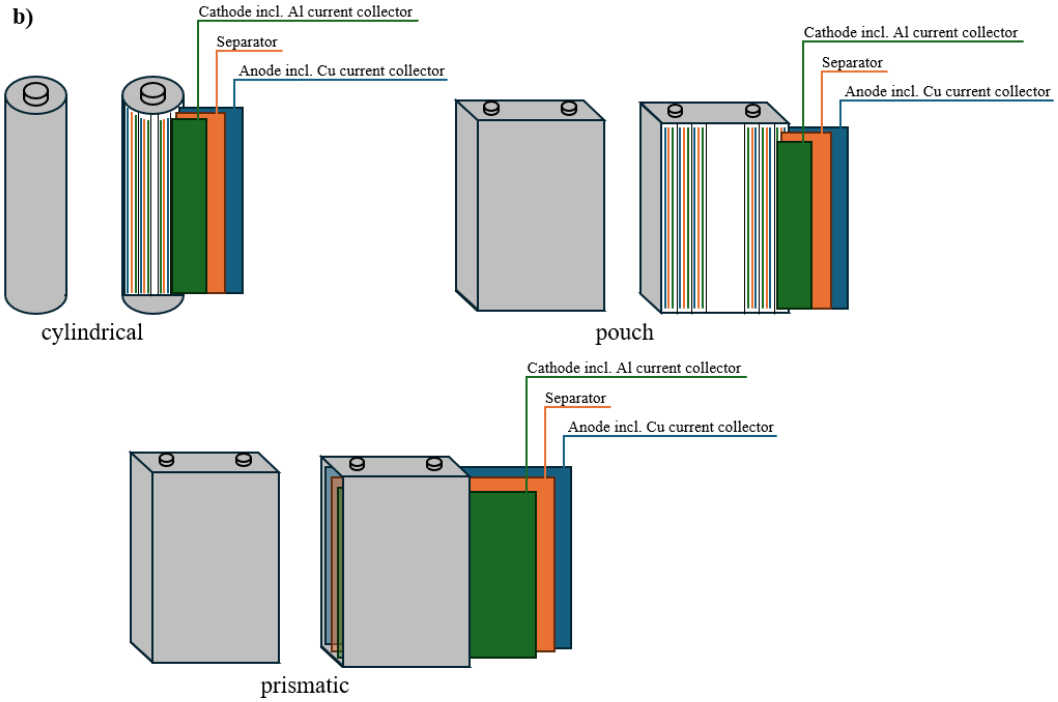

Figure 1 – Simplified overview of LIB structures (a) and cell design (b)

In general terms, the main components of LIBs cells are electrodes, binder, current collectors, separator, and electrolyte. They are sealed with either a plastic, steel or refined Al casing, with Al being the preferred material (Bhar et al., 2023; Yu et al., 2023).

The chemical composition of the cathode electrode is strongly determined by the battery application and the required characteristics (Windisch-Kern et al., 2022; Yu et al., 2023). The following cathode compositions are commonly used in EVs: $LiNi_xMn_yCo_{1-x-y}O_2$ (NMC), $LiMn_2O_4$ (LMO), $LiNi_xCo_yAl_{1-x-y}O_2$ (NCA), and $LiFePO_4$ (LFP) (DERA, 2021; Z. Yang et al., 2022). The subscripted numbers and variables within the cathode chemistry indicate the molar ratio between transitional metals and thereby determining the battery characteristics (Kim et al., 2020; Windisch-Kern et al., 2022). The frequently used transitional metals in EVs are Co, Mn, and Ni metal cations, as they enhance the rate capability, safety, and energy density of LIBs, respectively (Kim et al., 2020; Wen et al., 2020; Z. Yang et al., 2022). NMC being the most popular cathode chemistry, stoichiometry variations of transitional metals have become more apparent over time. High Co containing cathode electrodes, such as LCO and NMC111, have incentivized the development and increased the application of NMC622 and NMC811, where the numbers indicate the molar ratio between Ni, Mn, and Co, respectively (DERA, 2021; Windisch-Kern et al., 2022). This is due to growing demand for higher energy density LIBs, but most importantly because of the high costs, ethnical conflicts and supply risks associated with the Co extraction (DERA, 2021; Ruismäki et al., 2020).

The anode electrode in LIBs is largely made of Graphite (Windisch-Kern et al., 2022). The carbon allotrope possesses non-metallic properties, while still providing the electrical conductivity, high thermal and mechanical stability, and long-term cycle stability required for LIBs (Baum et al., 2022; MWI, Inc., 2023; Vasumathi et al., 2023). The latter characteristics are explained by the strong interlayer bonds and weak van der Waals bonds between the Graphite planes, making it possible for electrons to move freely within these layers (MWI, Inc., 2023; Vasumathi et al., 2023; H. Zhang et al., 2021). Additionally, this attribute allows for Graphite layers to expand and contract during the repeated charging and discharging, during which Li^+ ions migrate into and out of the graphite layers, without compromising the structural integrity of Graphite (H. Zhang et al., 2021). Among the Graphite types, naturally flaked and synthetic Graphite are most commonly used in EV-LIBs due to their high purity and structural forms, which have positive effects on the energy storage, electrical conductivity, and overall battery performance (Moradi & Botte, 2016; Vasumathi et al., 2023; H. Zhang et al., 2021).

Another component of LIBs are polymer binders, often polyvinylidene fluoride (PVDF), which act as glue between electrodes and current collectors (Yu et al., 2023). The current collectors are made of conductive metal foils with Cu and Al for anode and cathode, respectively (Bhar et al., 2023). An ion-permeable separator consists of a microporous membrane and the common material is polyolefins, including polyethylene and polypropylene (Brückner et al., 2020; Yu et al., 2023). The separator is crucial as it allows Li^+ ions to pass between the electrodes during charging and discharging of LIBs, while inhibiting a short-circuit caused by the contact of cathode and anode layers (Chernyaev et al., 2024; Yu et al., 2023). Lastly, lithium salts dissolved in organic carbonate-based solution, commonly $LiPF_6$ and ethylene carbonate, respectively, serve as the liquid electrolyte (Chernyaev et al., 2024; Yu et al., 2023).

Charging and discharging LIBs is a process based on the electrochemical principle of converting electrical to chemical energy and vice versa during discharging (Xie & Lu, 2020). During charging, or intercalation, Li^+ ions are extracted from the lattice structure of the cathode material to maintain charge neutrality as a result of the applied electrical energy. The extracted Li^+ ions are solvated by the electrolyte and migrate through the porous separator to the anode. There, Li^+ ions settle inside Graphite layers and thus form Lithiated graphite, LiC_6 (Bhar et al., 2023; Xie & Lu, 2020). During discharging, or deintercalation, Li^+ ions move back to the donor electrode, the cathode, while electrons are delivered to an external circuit. This reversed reaction indicates that stored chemical energy is converted back to electrical energy (Bhar et al., 2023; Xie & Lu, 2020). This process is also known as the rocking chair principle, due to the continuous back and forth movement

of Li^+ ions (Xie & Lu, 2020). The intercalation of Li^+ ions during charging is illustrated in the following Figure 2.

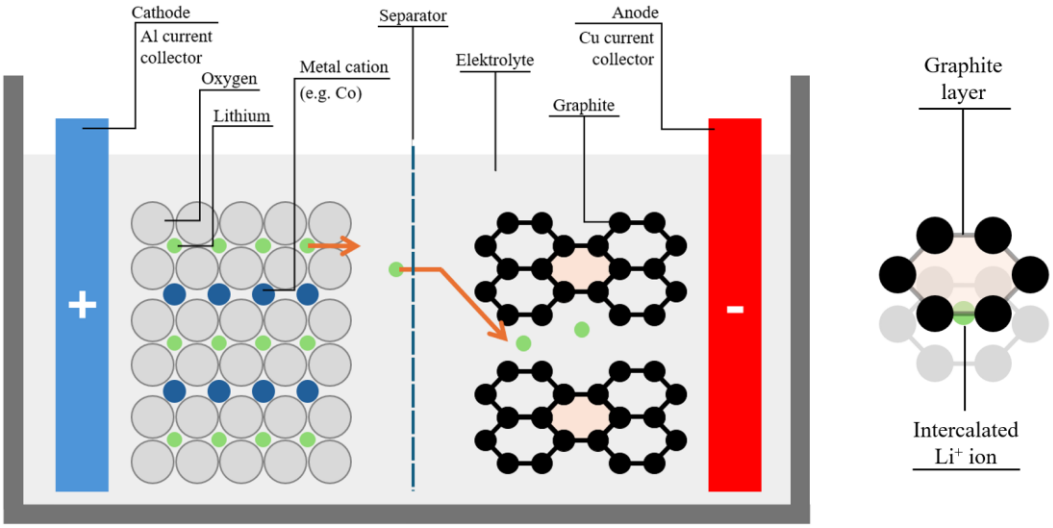

Figure 2 – Overview of LIB cells during charging/ Li^+ ion intercalation

The chemical reaction of this process can be generalized to the following reaction, where M stands for a possible cathodic transitional metal:

$$C_6 + LiMO_2 \leftrightarrow Li_xC_6 + Li_{(1-x)}MO_2$$

Over time, when the battery capacity of LIBs decreases to 70 – 80 %, which generally occurs after 5 – 8 years, the LIBs must retire out of safety reason and are therefore recycled or reused (Lai et al., 2022). Considering the massive number of EV-LIBs being produced yearly, the LIB waste amount is expected to rise immensely in the coming years (Baum et al., 2022). The International Energy Agency anticipates a total waste amount of 8 million tons by 2040, while other studies have also reported a total waste amount of 6.76 million tons by 2035 (Liu et al., 2022; Stone, 2021). If SLIBs are not recycled or reused, the excessive waste amount could lead to detrimental environmental issues, including air and water pollution, and the depletion of raw material reserves (Baum et al., 2022). Thus, the EU has set a minimum collection rate of SLIBs of 70 % by the end of 2030, with a 95 % recycling rate for valuable metals, including Co, Cu, and Ni, and a 70 % recycling rate for Li (Windisch-Kern et al., 2022). This directive is set to improve the environmental impacts and resource depletion of LIB production and recycling (Lai et al., 2022).

2.2 Recycling of SLIBs

Recycling SLIBs is critical due to the valuable materials they contain, and the environmental hazards associated with the improper disposal of SLIBs (Lai et al., 2022). The primary recycling routes currently applied in the industry are direct physical, pyrometallurgical, and hydrometallurgical processes (Wagner-Wenz et al., 2023). These

methods aim to recover valuable metals, such as Co, Cu, and Ni (Rey et al., 2021; Thompson et al., 2020). The following Figure 3 presents a general overview of the mentioned recycling routes and their foundational steps:

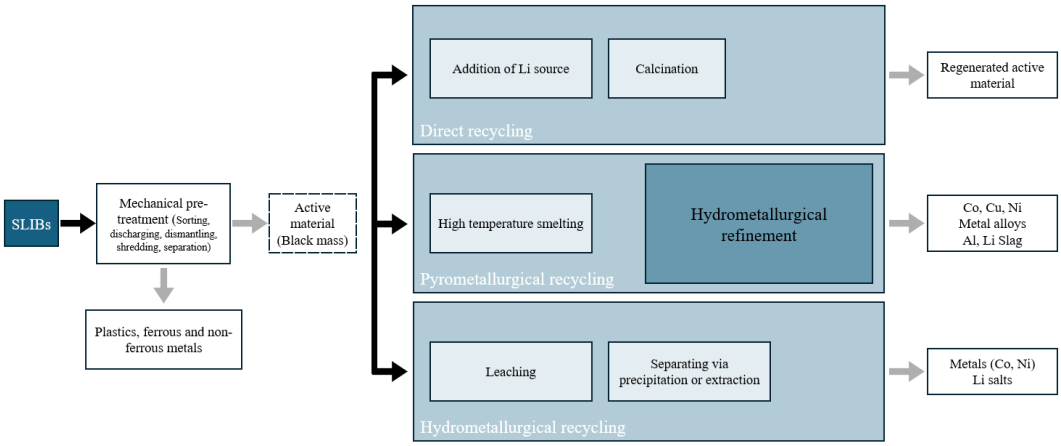

Figure 3 – Overview of recycling routes of SLIBs

Among these routes, the mechanical pretreatment is notable for producing what is known as “black mass”, or active material. This intermediate product consists of finely ground materials, including active cathode and anode materials, which are rich in Graphite and valuable metals like Co, Li, Mn, and Ni (Vanderbruggen, 2022). The extraction and purification of these metals from the active material are essential steps in the recycling process, making it a focal point in LIB recycling (Vanderbruggen, 2022). Thus, the active material produced during the mechanical pretreatment is commonly the starting material for the recycling processes (Wagner-Wenz et al., 2023).

2.2.1 Mechanical Pretreatment Steps

The mechanical pretreatment of SLIBs is often a prerequisite for recycling SLIBs, since the complex structure and the abundance of materials used in LIBs pose challenges during subsequent recycling processes (Yu et al., 2023). The mechanical pretreatment allows for a larger number of secondary resources to be recovered with high purities, while regarding economic aspects (DERA, 2021; Rinne et al., 2022; Velázquez-Martínez et al., 2019).

Considering the variety of cathode chemistry in EV-LIBs, classifying and sorting SLIBs prior to pretreatments is required to decide on a suitable and economic viable recycling route, since each cathode composition requires different recycling processes to extract the valuable metals (Rinne et al., 2022; Yu et al., 2023). Additionally, SLIBs are sorted by the state-of-health to determine good performing LIBs, which are refurbished for second-life-applications in EVs and energy storage systems (Windisch-Kern et al., 2022; Yu et al., 2023). The low performing SLIBs, otherwise known as end-of-life batteries, are discharged and dismantled into battery modules and its housing components before being subjected to mechanical pretreatments (Bhar et al., 2023; Windisch-Kern et al., 2022; Yu et al., 2023).

Discharging via conductive solutions or thermal deactivation is a crucial step to enhance the safety during dismantling and the following mechanical treatments, since mechanical or electrical impacts can lead to internal short-circuits and explosions due to the remaining electric energy and flammable liquid electrolyte in LIBs (Bhar et al., 2023; Yu et al., 2023). By dismantling SLIBs prior to mechanical pretreatments, materials used in LIB housings can be removed and recovered, which positively influences the recycling efficiency, since reducing the volume and its variety of materials increases the recycling output (Windisch-Kern et al., 2022; Yu et al., 2023).

In the subsequent mechanical pretreatment, SLIB modules are crushed and sieved, in order to liberate and separate remaining materials based on their physical properties into concentrates (Brückner et al., 2020; Ruismäki et al., 2020). While Al and Cu are found in coarse fractions, the resulting active material is fine fractioned and contains mainly electrode materials (Rinne et al., 2022; Windisch-Kern et al., 2022). By introducing mechanical pretreatment steps, the desired materials can be separated from contaminants in a more targeted manner (Bhar et al., 2023). However, impurities found in active material, especially organic binders, electrolyte residues and current collector fractions, pose difficulties in further processing individual materials during metallurgical treatments (Vanderbruggen et al., 2021; Yu et al., 2023).

At this part of the process, thermal treatment and froth flotation can eliminate the above-mentioned impurities and separate the active material in order to enhance the subsequent recovery outcome of individual materials (Vanderbruggen et al., 2021; Yu et al., 2023). By implementing a thermal treatment at 400 – 600 °C, the organic components decompose, thereby liberating the active material surfaces for the following froth flotation (Brückner et al., 2020; G. Zhang et al., 2021). Seeing as froth flotation is based on the hydrophobic and hydrophilic differences between materials, hence the surface chemical properties, the surface of the feed material should be liberated from impurities, which would otherwise negatively influence the hydrophobic and hydrophilic properties of the single feed components (Pawlik, 2022; Vanderbruggen et al., 2021).

During froth flotation, the hydrophobic material attaches to air bubbles and rises to the froth layer, while hydrophilic particles sink to the pulp layer. This process is commonly influenced by adding reagents, such as frothers and collectors (Pawlik, 2022). These surface-active agents modify the interfacial properties of the particles with the help of their heteropolar ends. Collectors, derived from water-insoluble oils, selectively coat hydrophobic particles and improve the true flotation behavior of the selected minerals, thereby making them more hydrophobic (Pawlik, 2022). Frothers, on the other hand, are designed to stabilize the froth layer by decreasing the surface tension of water (Pawlik,

2022; Vasumathi et al., 2023). A stable froth is crucial for collecting the hydrophobic minerals, as the froth should not be ruptured while removing the froth (Pawlik, 2022). Additional to the reagents, operational factors, such as airflow rate and agitation, play a crucial role in froth flotation (Wang & Liu, 2021). The airflow rate is essential for the generation of air bubbles that collect the hydrophobic particles and produce a concentrated froth layer (Vanderbruggen et al., 2021). The proper agitation is induced by the rotating impellers, which distributes the air bubbles and contributes to the bubble-particle interaction, necessary for the collision of air bubbles and hydrophobic particles (Vanderbruggen et al., 2021; Wang & Liu, 2021). The resulting froth and pulp products can then be subjected to hydrometallurgical processes for the recovery of battery-grade electrode material (Vanderbruggen, 2022). By separating the active material, the material volume and solvent consumption used during hydrometallurgy can be reduced, while the recycling yield can be increased (Vanderbruggen, 2022; Windisch-Kern et al., 2022).

2.2.2 Metallurgical Recycling Processes

Following the previously mentioned mechanical pretreatment steps, the concentrates are subjected to metallurgical routes in order to purify and recover battery-grade materials (Brückner et al., 2020; Velázquez-Martínez et al., 2019).

Traditional metallurgical methods can be divided into pyrometallurgical and hydrometallurgical processes. Pyrometallurgical routes, such as roasting and reduction processes, apply high temperatures to induce oxidization or reduction reactions, respectively (Windisch-Kern et al., 2022). Regarding LIBs, the resulting metal alloys contain Co, Cu, and Ni, whilst the generated slag consists of Al and Li (Baum et al., 2022; Bhar et al., 2023). However, with these methods, carbon oxidizes or is used as a reduction agent, which prevents Graphite from being recycled (Brückner et al., 2020; Windisch-Kern et al., 2022). Furthermore, the recovered alloy and slag have to be hydrometallurgically refined in order to obtain battery-grade metals (Ma et al., 2023; Windisch-Kern et al., 2022). While pyrometallurgical routes are cost-efficient and allow a larger capacity of SLIBs to be processed, the required amount of energy and the gas pollution to the atmosphere have to be considered from an environmental standpoint (Ma et al., 2023; Rey et al., 2021). On an industrial scale, SLIBs are commonly fed into pyrometallurgical routes without prior mechanical pretreatments, as the additional pretreatment steps would lead to higher costs (Z. Yang et al., 2022). Thus, a larger number of materials is lost during pyrometallurgical processes, including Al, Li, and Graphite (Z. Yang et al., 2022).

Hydrometallurgical methods usually include leaching, extraction and separation of metals into solution, followed by final precipitation or extraction stages (Lai et al., 2022; Wagner-Wenz et al., 2023). Compared to pyrometallurgy, this method achieves a higher purity and

recovery rate in the recycling of secondary materials (Ma et al., 2023). Nonetheless, the large amount of leachates, and water required during these complicated treatments makes hydrometallurgy a costly option, especially on a larger industrial scale (Ma et al., 2023; Velázquez-Martínez et al., 2019). To reduce the amount of leachate and water, Graphite should be removed before hydrometallurgical treatments, since the initial material volume is thereby reduced. (Ma et al., 2023; Vanderbruggen et al., 2022). A further challenge in hydrometallurgical processes is the disposal of untreated liquid waste with possible heavy metal contamination, which detrimentally burdens the environment with its secondary pollution (Baum et al., 2022; Ma et al., 2023; Rey et al., 2021).

On an industrial scale, pyrometallurgy with following hydrometallurgy methods is the most applied route for recovering materials from SLIBs, since it allows the purification and recovery of batter-grade metals (Baum et al., 2022).

3 Materials & Methods

Chapter 2 details the materials and methods utilized in this study, including the active materials and simulated froth flotation materials, foundational descriptions of XRD and SEM-EDS analyses, sample preparation, diffraction pattern analysis, and the presentation of the simulated froth flotation using a self-built flotation cell.

3.1 Materials

The active material sample used in this study, as shown in Figure 4, stem from EV-SLIBs, in which NMC and Graphite were the main cathode and anode materials, respectively. To investigate the elemental and mineralogical phase composition of the active material used in this study, XRD and SEM-EDS measurements were carried out to characterize the components of the active material and any impurities it may contain. Since the active material was provided by an anonymous supplier, information on the exact composition ratio and potential mechanical and thermal pretreatment steps of the active material is unknown due to confidentiality agreements of the supplier and their suppliers. Nonetheless, based on the XRD and SEM-EDS results, conclusions can be drawn regarding the composition of electrode materials, the presence of impurities, such as organic binder, electrolyte, and current collectors, and the potential pretreatment steps applied to the active material.

Figure 4 - Active material sample

The sample mass for the simulated froth flotation was 42.5 g and the reagents employed were N-dodecane as a collector and MIBC as a frother. The concentration of the collector and frother were approximately 300 g/t and 150 g/t, respectively (G. Zhang et al., 2018).

3.2 Methods

The initial analysis of the material composition of the active material was conducted using XRD. However, due to the presence of multiple phases in active materials and the lack of information on material components and pretreatment steps, the XRD measurements alone did not suffice for a proper elemental and phase identification of the active material investigated in this study. Thus, SEM-EDS measurements were performed to characterize the elements present in the samples. With the provided information from SEM-EDS measurements, the XRD results were reviewed and analyzed in a more precise manner. In the following Subchapters, 3.2.1, and 3.2.2, the fundamental principles of both methods of analysis are explained.

During the characterization of the samples by XRD, it was noticeable that the measured diffraction patterns contained multiple diffraction patterns. To further improve the XRD characterization, a simulated froth flotation was introduced to reduce the phases present in the samples, which would in turn improve the XRD characterization. The simulated froth flotation process is described in more detail in Subchapter 3.2.3.

In Figure 5, two flowcharts are shown: Workflow 1, summarizing the overall workflow of the study, and Workflow 2, detailing the process steps followed during the simulated froth flotation.

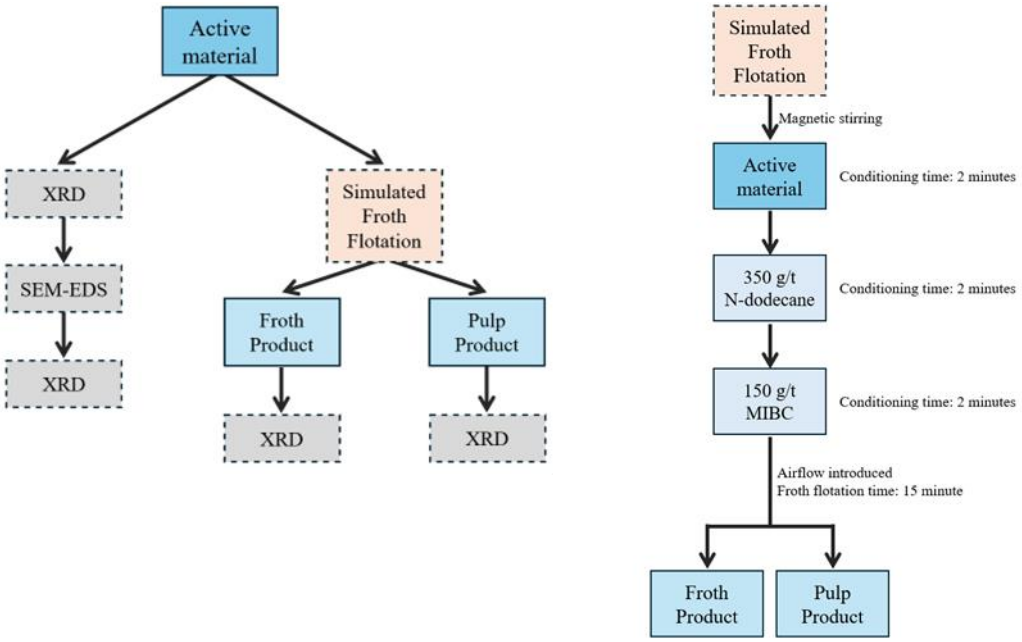

Figure 5 – Flowchart of Workflow 1 (left) and Workflow 2 (right)

3.2.1 XRD

XRD utilizes the characteristic diffraction of X-rays by crystals to precisely determine the structure of crystalline phases, without destructing the sample structure throughout the process (Epp, 2016).

In essence, X-rays in XRD measurements are generated by electrons. These electrons, emitted from a heated tungsten filament, are accelerated towards an anode target, typically made of a metal such as Cu (Epp, 2016). When the accelerated electron collides with the targeted anode, X-rays are produced by two effects. The first effect is the deceleration of the electron, which emits X-ray photons with a continuous emission spectrum, also referred to as "*Bremsstrahlung*" (Epp, 2016). The second effect is induced by the electron knocking out an inner shell, or K shell (n = 1), electron from the targeted anode, causing ionization (Epp, 2016). This creates a vacancy within the inner shell that is filled with an outer shell electron with higher energy levels. During this relaxation, energy is released in the form of characteristic X-rays. If an electron from the next outer shell, or L shell (n = 2), fills the vacancy, it is referred to as K_α-transition, whereas electrons coming from the M shell result in K_β-transition (Lee, 2017). The generated X-rays are then filtered for the high intensity K_α radiations, and emitted as monochromatic X-rays from the X-ray tube towards the sample to be analyzed (Bunaciu et al., 2015).

When samples with crystalline structures are analyzed, the incident X-rays are scattered constructively or destructively, depending on the periodic nature of the crystalline structure. XRD is thus a method based on the diffraction of X-rays by the periodically arranged atoms in the crystal and the measurement of the diffracted signal by angle or

energy (Chauhan & Chauhan, 2014; Epp, 2016). However, only by the constructive interference of the incident and the reflected X-rays, which occurs at angles satisfying the Bragg's Law, the diffracted X-rays can be detected (Chauhan & Chauhan, 2014). With the measured diffraction angles, the interplanar distance, *d*, can be calculated by using Bragg's law, expressed as:

$$n\lambda = 2d \sin\theta$$

where *n* is an integer referring to the order of reflection, λ is the wavelength of the X-rays, d is the interplanar distance, and θ is the diffraction angle. It should be noted that the Bragg's angle and the detected 2θ angles are not the same, as the Bragg's angle refers to the angle between the sample and the X-ray source and the 2θ angle to the angle between the incident X-ray and the detector (Ravi Sharma et al., 2012).

The diffraction of X-rays by crystals results in patterns that are characteristic of the structure of the crystals in question. This is due to the fact that the interplanar distance affects the diffraction pattern (Chauhan & Chauhan, 2014). Therefore, the resulting diffraction pattern of a crystallographic phase can be considered their unique fingerprint (Bunaciu et al., 2015; Marinescu, 2000).

The resulting diffraction pattern, otherwise known as diffractogram, plots the measured intensity against the detected angle 2θ (Chauhan & Chauhan, 2014). The unit cell's size and shape of the crystallographic phase determines the position of the diffraction peak, thus provides information on the crystalline space group and the lattice plane, characterized by the Miller index (Chauhan & Chauhan, 2014). The areas under the diffraction peaks are determined by the number of phases present in the samples. Thus, information on the mineralogical phase composition of the sample can be retrieved by XRD analysis (Ravi Sharma et al., 2012). The broadening of diffraction peaks can be attributed to many reasons, including the presence of defects in the crystalline structure, differences in lattice spacing, and the size of crystallites. Additionally, amorphous structures can lead to distorted diffraction patterns, thus influencing the phase composition analysis (Chauhan & Chauhan, 2014).

The XRD analysis in this study was performed with the Huber G670 powder diffraction (HUBER Diffraktionstechnik GmbH & Co. KG) using a Cu K_α X-ray radiation source (λ = 1.54178 Å, 30 kV, 40 mA). Each XRD measurement duration was 60 minutes.

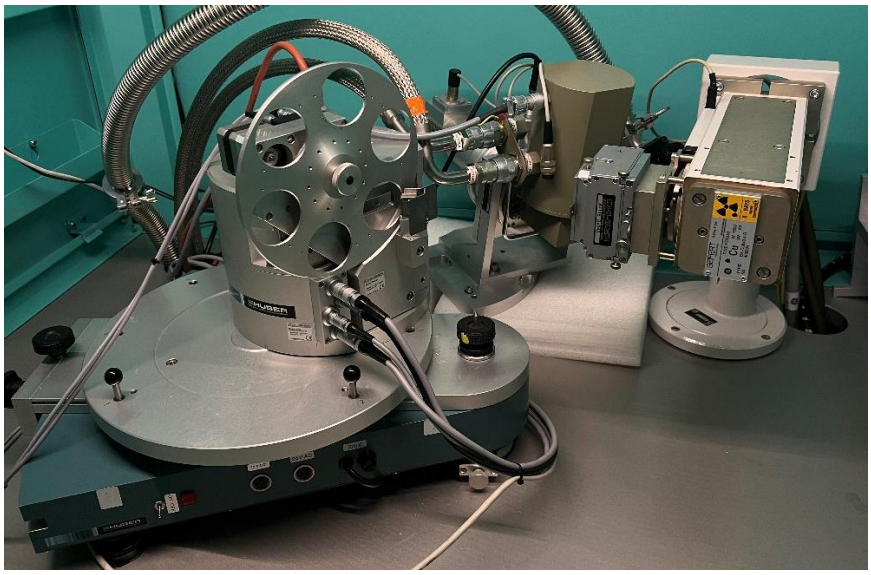

Figure 6 – Huber G670 powder diffraction

3.2.1.1 Sample Preparation

For a conclusive XRD characterization of the active material samples, the samples were first mortared for approximately 2 minutes to ensure that the samples were finely powered. The samples were then applied to the sample holder by fixing them between two transparent foils, as shown in Figure 7. During the application of the samples, it was important to distribute the samples evenly and no excessive external pressure was applied that could change the orientation of the containing mineralogical phases, which could lead to inaccurate results.

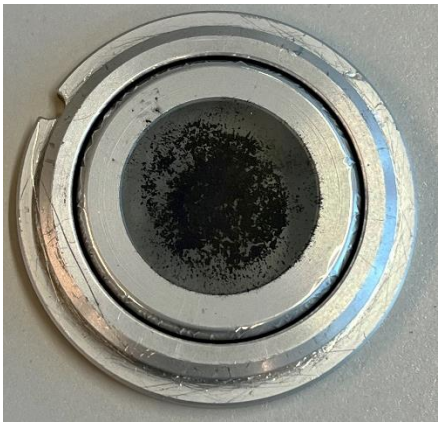

Figure 7 – Sample holder with active material between two transparent foils

3.2.1.2 Analysis of XRD Patterns

In order to accurately analyze the XRD results, the diffraction patterns were evaluated using the software MATCH 3- Powder Diffractogram Analysis by Crystal Impact. For this analysis, the diffraction patterns had to be revised by first adjusting the baseline manually. If the diffraction patterns exhibited high background noise, setting the baseline could lead

to diffraction peaks with lower intensities being overlooked. Consequently, certain mineralogical phases may not be completely determined in the subsequent analysis. While the software was able to identify diffraction peaks with high intensities, many of the remaining peaks had to be identified and added manually. To improve the identification of lower intensity peaks, three measurements of the active material samples, and four measurements of each of the froth flotation products were taken, and their resulting diffraction patterns were compared. An example can be seen in Figure 8. This approach allowed for better determination of low intensity diffraction peaks at similar 2θ angles. The finalized diffraction patterns, with the adjusted baseline and identified peaks, is referred to as the "calculated diffraction pattern".

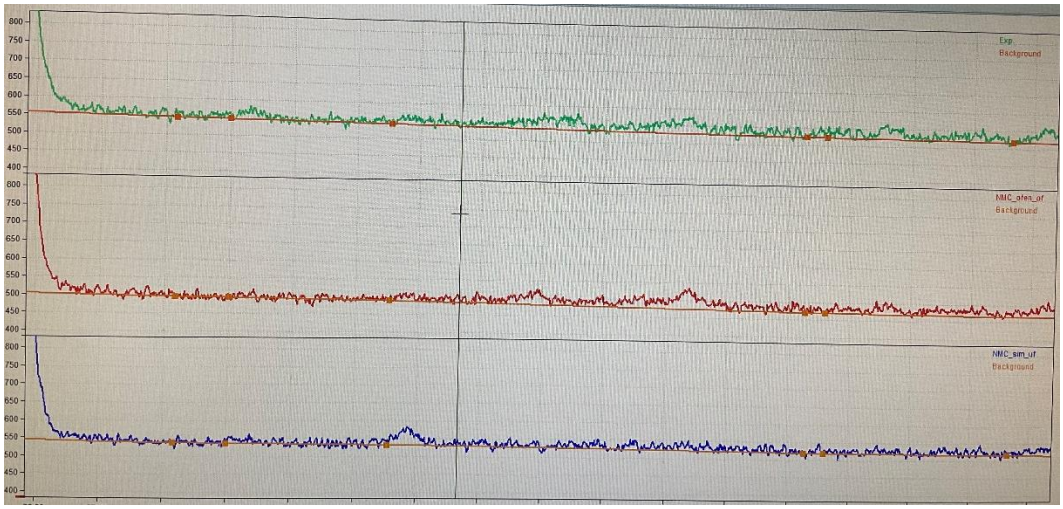

Figure 8 – Example of measurement comparison for diffraction peak identification

Based on the calculated diffraction pattern, the last step in analyzing the XRD results required matching potential mineralogical phases to the calculated diffraction patterns. To achieve an accurate analysis, three approaches were employed simultaneously: restricting the element selection, comparing the diffraction patterns, and evaluating the figure of merit (FoM). The selection of elements was narrowed down to those that appeared in the result of the SEM-EDS analysis and the literature research. This restriction allowed the software's automatic search to limit on the mineralogical phases likely present in the active material. When comparing the simulated diffraction patterns of the mineralogical phases with the calculated diffraction patterns, distinctive diffraction peaks with high intensities of the potential phases were taken into consideration. The simulated diffraction patterns of the mineralogical phases matched to the active material can be found in the Supplementary Information, S1. Lastly, the FoM provided by the software, which is explained in simple terms due to the limited scope of this study, describes how well the simulated diffraction pattern fits to the calculated diffraction pattern based on the intensity, width, 2θ angle of the diffraction peaks.

When assigning the diffraction peaks to the suitable mineralogical phases, the order of matching significantly influenced the resulting mineralogical composition. This is due to the software subtracting the suggested intensity of the already matched mineralogical phase and continues to match the diffraction peaks with the remaining intensity in subsequent assignments. Thus, the automatic matching of further mineralogical phases to those diffraction peaks, especially with low intensities, can often result in mismatching and therefore lead to mistakes. For samples with multiple mineralogical phases present, the various mineralogical phases may present diffraction peaks at the same or similar 2θ angles. This could result in several mineralogical phases being assigned to a single diffraction peak which, as mentioned before, is prone to errors. Without the knowledge of the elements or phases present in the samples, the XRD characterization can become challenging. Therefore, the results of the SEM-EDS analysis and literature research were crucial for accurately assigning all diffraction peaks to the corresponding elements and their mineralogical phases. The order of matching the mineralogical phases was based on the following steps: First, the four diffraction peaks with the highest intensities were selected and matched to possible mineralogical phases. Second, the selection of possible mineralogical phases was refined based on the FoM. And lastly, certain mineralogical phases identified through literature research were added manually to the selection and compared with the calculated diffraction patterns. This approach allowed the remaining calculated diffraction peaks to be accurately assigned.

3.2.2 SEM-EDS

For a better understanding, SEM and optical microscopy can be compared. While optical microscopy applies light to obtain magnified images of samples, SEM applies electrons and a series of electromagnetic lenses, thus achieving a magnification of more than 300,000x, compared to 400 – 1000x in optical lenses (O'driscoll, 2023). SEM utilizes an electron gun that generates a high-energy electron beam to scan the sample in a raster pattern to obtain topographical, morphological and crystallographic information (Girão et al., 2017; O'driscoll, 2023).

When beam electrons hit and intrude the sample, they interact with the electrons within the sample, through which characteristic X-rays, secondary, and backscattered electrons can be measured among the many more interactions that occur. Secondary and backscattered electrons are responsible for producing the SEM mapping, whereas the characteristic X-rays are utilized for the EDS analysis. Secondary electrons are generated when a beam electron collides with a sample electron, after which its course is changed, and its energy is largely transferred to the sample electron, thereby significantly reducing the energy level of the initial beam electron. This effect is also called inelastic scattering or interaction

between beam and sample electrons, as the kinetic energy is largely transferred (Girão et al., 2017; Thermo Fischer Scientific, n.d.–b). Backscattered electrons are generated when a beam electron also collides with a sample electron, but are reflected by approximately 180 °, while losing a small part of its energy. This is referred to as elastic scattering or interaction, as the kinetic energy is mostly retained after the beam and sample electron interaction. Secondary electrons provide surface structure information, while backscattered electrons deliver compositional (atomic number) information of the sample. This is because secondary electrons originate from the sample surfaces, while the backscattered electrons originate from a deeper point of the sample, explaining their provided information on the sample (Thermo Fischer Scientific, n.d.–b). Backscattering electrons provide compositional information based on the atomic number of the sample, since elements with a higher atomic number generate more backscattering electrons compared to elements with a lower atomic number (University of Cambridge, n.d.). This is called the atomic scattering factor and is related to the higher charge density of the elements, thus the higher atomic number, Z (Thermo Fischer Scientific, n.d.–b). Both electron types are detected by a secondary electron and backscattering electron detector for the respective electron type (Girão et al., 2017).

As previously mentioned, X-rays are generated when beam electrons hit the sample. With the help of EDS analysis, the emitted X-rays from the sample are detected by their intensity and its energy (Gaston & Protter, 2019). The provided information on the sample is then presented in an energy spectrum that can be analyzed based on the element and its quantities (Thermo Fischer Scientific, n.d.–a). By combining SEM and EDS, a powerful analysis tool is thereby created, which allows the identification of surface structure and element composition.

The SEM-EDS analysis in this study was done using the REM Thermo Fisher Prisma E (Thermo Fisher Scientific Inc.). The SEM-EDS measurements done in this study were based on the secondary electrons measured by an Evenhart-Thornley Detector and at a magnification scale of 1 mm.

3.2.3 Simulated Froth Flotation Procedure

The simulated froth flotation procedure in this study was carried out in a self-built flotation cell, as shown in Figure 9. The self-built flotation cell had a tube with small holes poked horizontally on the sides, which provided the necessary airflow of nitrogen. To ensure the agitation, a magnetic stirrer and three magnetic stirring sticks were utilized as a substitute for the impeller found in conventional froth flotation cells.

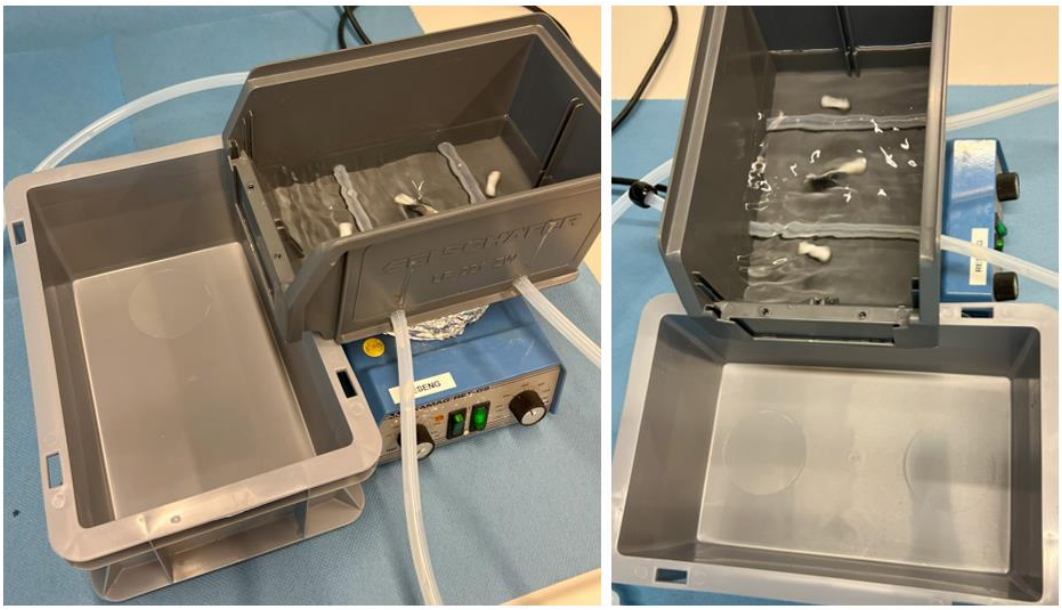

Figure 9 – Simulated froth flotation in the self-built flotation cell

The simulated froth flotation procedure in this study imitates the actual froth flotation steps. At first, 42.5 g of active material and 850 mL of tab water were added to the flotation cell, followed by a conditioning time of 2 minutes during which stirring took place. This approach ensured a uniform distribution of the active material sample within the flotation cell. Subsequently, N-dodecane was added as collector with a dosage of approximately 300 g/t and conditioned for 2 minutes under the same stirring conditions. Afterwards, approximately 150 g/t MIBC as frother was introduced with a conditioning time of 2 minutes, also under identical stirring conditions. Lastly, nitrogen was introduced to the flotation cell, initiating the froth flotation process. The simulated flotation process was carried out until the froth amount and bubble size visually decreased significantly, which occurred after 15 minutes. To obtain the froth during the procedure, the froth was continuously scrapped off the flotation cell using a plastic cover and transferred into a plastic box set below the flotation cell, as can be seen in Figure 9. The pulp product was retrieved by transferring the remaining material in the flotation cell into separate beakers. After the simulated flotation, the collected froth and pulp products were dried in a convection oven (Binder FP 115) for 3 hours at 120 °C. However, both products did not dry completely, which is why the products were placed in a fume hood until they were completely dry. To prepare the dry froth flotation products for the subsequent analyses, the products were mortared for 2 minutes until there were no noticeable coarse fractions.

4 Results & Discussion

The results and discussion section presents and analyzes the material composition of the active material using XRD and SEM-EDS techniques, as well as the material composition of froth flotation products using XRD, to address the RQ posed in this study. Additionally, the fundamental effectiveness of the simulated froth flotation is discussed as a part of the RQ.

4.1 SEM-EDS and XRD Characterization of NMC Active Material

4.1.1 SEM-EDS

The SEM-EDS results of the three measurements on the elemental composition of the NMC active material are presented in Tables 1 and 2. Additionally, a detailed SEM-EDS mapping showing individual particles of Al, Cu and Si is provided in Figure 10. Further SEM-EDS mappings of all three samples are available in the Supplementary Information, S2.

Element	Atomic Percentage (%)			Mean Value	Standard deviation
Sample	1	2	3		
Al	3.60	3.30	3.50	3.47	0.12
C	60.10	60.90	59.50	60.17	0.57
Ca	0.10	0.10	0.10	0.10	0.00
Cl	0.10	0.10	0.10	0.10	0.00
Co	5.80	5.70	6.00	5.83	0.12
Cu	0.40	0.40	0.40	0.40	0.00
Mg	0.10	-	0.10	0.10	0.00
Mn	1.70	1.70	1.80	1.73	0.05
Ni	1.60	1.60	1.70	1.63	0.05
O	25.60	25.40	25.80	25.60	0.16
P	0.50	0.50	0.50	0.50	0.00
S	0.10	0.10	-	0.10	0.00
Si	0.30	0.30	0.40	0.33	0.05

Table 1 – Elemental composition in atomic percentage from SEM-EDS analysis

Element	Weight Percentage (%)			Mean Value	Standard deviation
Sample	1	2	3		
Al	5.30	5.00	5.10	5.13	0.12
C	39.60	40.50	38.80	39.63	0.69
Ca	0.30	0.30	0.30	0.30	0.00
Cl	0.20	0.20	0.20	0.20	0.00
Co	18.90	18.60	19.10	18.87	0.21
Cu	1.20	1.30	1.30	1.27	0.05
Mg	0.20	-	0.20	0.20	0.00
Mn	5.30	5.20	5.50	5.33	0.12
Ni	5.30	5.20	5.50	5.33	0.12
O	22.50	22.50	22.40	22.47	0.05
P	0.80	0.80	0.80	0.80	0.00
S	0.10	0.10	-	0.10	0.00
Si	0.50	0.50	0.60	0.53	0.05

Table 2 – Elemental composition in weight percentage from SEM-EDS analysis

The results indicate that the majority of the elemental composition consists of Al, C, Co, Mn, Ni, and O, as highlighted in blue in Tables 1 and 2. Cu, P, and Si represent a smaller proportion, marked in orange in Tables 1 and 2. Elements such as Ca, Cl, Mg, and S had the smallest share, with atomic and weight percentages ≤ 0.2 %, and are therefore not considered relevant in this study.

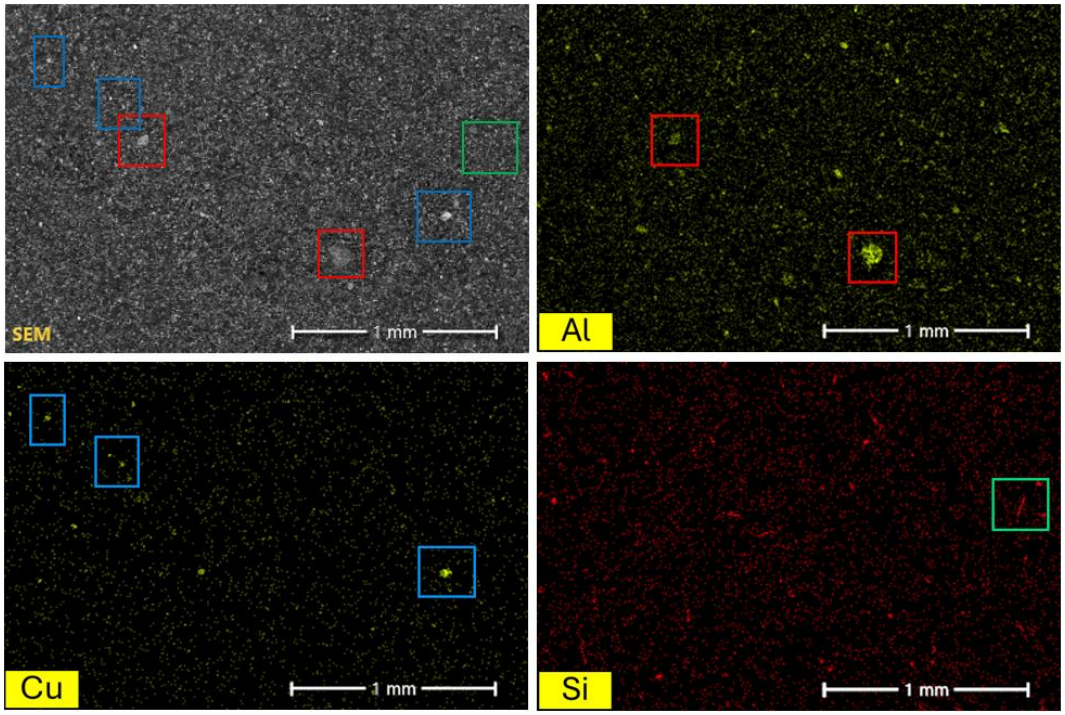

Figure 10 – SEM-EDS mapping of active material containing Al, Cu, and Si

The SEM-EDS mappings in S2 show a mostly homogeneous distribution of elements. While C, O, and Co covered a large area, Mn, Ni, and P were less detectable. Notably, individual particles of Al, Cu, and Si were clearly visible and are marked in red, blue, and green squares, respectively, in Figure 10.

The presence of C can be linked to Graphite, the primary material used in anodes for EV-LIBs. Co, Mn, and Ni found in the samples are components of the cathode material (DERA, 2021; Kim et al., 2020; Z. Yang et al., 2022). When comparing the ratio between the anode and cathode materials, Graphite has a significantly higher proportion compared to Co, Mn, and Ni. Though it must be mentioned that Co, Mn, and Ni occur in the cathode as metal oxides and therefore make up almost 40 % if O in the electrode materials are considered. Thus, the approximate 60:40 ration between Graphite and the electrode materials measured in the samples is consistent with the typical EV-LIB composition (Vanderbruggen et al., 2021). Co appeared in higher proportions, suggesting a high-Co cathode composition, though this requires further verification with XRD analysis. Although Li is expected in the samples, Li cannot be measured with conventional SEM-EDS due to its low atomic number (Z = 3). The emitted characteristic X-rays of Li produce low energy of 55 eV, which are too weak and difficult to be measured with standard SEM-EDS detectors, therefore the presence of Li can neither be confirmed nor refuted solely based on the SEM-EDS analysis.

The high O content in the samples suggests the presence of metal oxides, which was expected due to the presence of Co, Mn, and Ni in the initial cathode material composition. However, further analysis with XRD is required to confirm the source of the high O

content. The high share of O also suggests that the samples were thermally treated, potentially causing other elements to react with O and increasing its content.

Al and Cu particles, marked in red and blue in Figure 10, were larger compared to other elements. Literature reports that Al and Cu are often found in coarse fractions in the active material, which is confirmed by the SEM-EDS mapping (Vanderbruggen, 2022). Al appeared in higher concentrations, likely due to its use in both current collectors and cell casing, while Cu is primarily used in current collectors (Bhar et al., 2023). This suggests that either entire battery cell units were treated without separating individual components, current collectors were not completely removed before recycling, or Al and Cu impurities remained from pretreatment processes.

Si particles, marked in green in Figure 10, were scattered in the samples, though the total atomic percentage of Si was only 0.3 %. The presence of Si cannot be explained by the standard material composition of LIBs and is likely due to contamination during LIB production or mechanical pretreatment. Other studies have identified glass fiber-shaped Si in active material but did not elaborate on its origin (Mousa et al., 2023).

The low proportion of P suggests it originated from the electrolyte ($LiPF_6$) and did not fully evaporate during thermal treatment (Yu et al., 2023). While studies indicate that electrolyte evaporation can be achieved at 300 °C, most thermal treatments of active material reach 500 – 600 °C, which should remove the electrolyte (Makuza et al., 2021). The residual P might result from the organic binder enveloping electrode particles and potentially retaining parts of the electrolyte. Although organic compounds tend to decompose at temperatures between 500 and 600 °C, complete decomposition cannot be guaranteed (Kriston et al., 2019; H. Yang et al., 2006; Yu et al., 2023).

In conclusion, the SEM-EDS analysis provided critical information on the phases expected in the subsequent XRD analysis. The presence of Co, Mn, and Ni, and the high O content suggests the formation of metal oxides, which are typical of NMC-based active material.

4.1.2 XRD

The diffraction patterns obtained from the XRD analysis of active material indicate the presence of several mineralogical phases. The composition of these phases is presented in Table 3, while the chemical composition, calculated from the mineralogical composition, is shown in Table 4. The diffraction patterns are presented in Figures 11 and 12. Figure 11 displays the most common phases found in the active material, including Al, Graphite, CoO, MnO, and Ni, which are colored blue in Tables 3 and 4. Figure 12 presents the remaining phases, such as Cu, $Li_2(CO_3)$, $LiAlO_2$, LiF, and SiO_2, with some low-intensity diffraction peaks marked in grey due to their weak matches. The XRD diffraction patterns

were analyzed with a focus on phases containing Al, Graphite, Co, Cu, Mn, Ni, O, P, and Si, based on SEM-EDS results, for more accurate phase identification.

Phase	Formula	Mineralogical Composition			Mean value	Standard deviation
Feed Material Samples		1	2	3		
Aluminum	Al	3.70	6.20	5.00	4.97	1.02
Graphite	C	41.40	52.10	50.20	48.00	4.71
Copper (II) oxide	CoO	3.70	4.10	4.00	3.93	0.17
Copper	Cu	1.60	1.40	1.60	1.53	0.09
Zabuyelite	$Li_2(CO_3)$	15.80	13.00	13.50	14.10	1.22
Lithium aluminum oxide	$LiAlO_2$	8.60	5.50	7.30	7.13	1.27
Lithium fluoride	LiF	6.90	5.90	6.80	6.53	0.45
Manganosite	MnO	3.50	3.10	2.80	3.13	0.29
Nickel	Ni	10.60	8.10	8.40	9.03	1.11
Cristobalite	SiO_2	4.10	0.70	0.60	1.80	1.63

Table 3 – Mineralogical phase composition of feed material from XRD analysis

The mineralogical composition showed that the majority of the sample consisted of Graphite, $Li_2(CO_3)$, and Ni, while Al, CoO, $LiAlO_2$, LiF, and MnO were less present. Cu and SiO_2 were found in traces.

Element	Chemical Composition (%)			Mean value	Standard deviation
Feed Material Samples	1	2	3		
Al	7.20	8.40	8.00	7.87	0.50
C	44.00	54.20	52.40	50.20	4.45
Co	2.90	3.20	3.10	3.07	0.12
Cu	1.60	1.40	1.60	1.53	0.09
F	5.00	4.30	5.00	4.77	0.33
Li	5.70	4.60	5.10	5.13	0.45
Mn	2.70	2.40	2.20	2.43	0.21
Ni	10.60	8.40	8.40	9.13	1.04
O	18.20	13.00	14.10	15.10	2.24
Si	1.90	0.30	0.30	0.83	0.75

Table 4 – Chemical composition of feed material from XRD analysis

The chemical composition indicated that C, Ni, and O were the most prevalent elements, while Al, Cu, F, Li, and Mn were present in lower amounts, and Cu and Si in traces. A comparison of the chemical composition to the SEM-EDS results will be presented in Chapter 4.1.3.

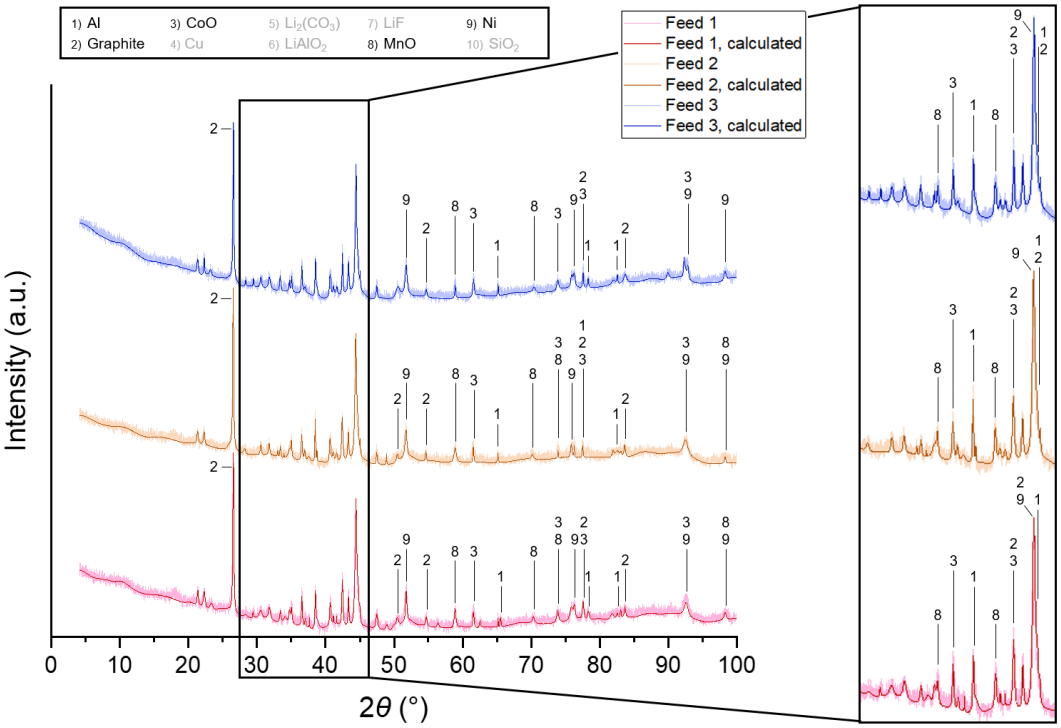

Figure 11 – Measured diffraction pattern of active material; Magnified view of diffraction pattern from 28 ° to 46 ° (right)

The order of phase matching impacted the mineralogical composition, as mentioned in Chapter 3.2.1.2.

Following the first step during phase matching, the four diffraction peaks with the highest intensities at approximately 26.5 °, 38.4 °, 42.4 °, and 44.4 ° were examined. As they were present in all three measurements, the primary phases identified were consistently Al, Graphite, and Ni.

The matching of CoO and MnO was based on the provided FoM, as the corresponding diffraction peaks in the calculated diffraction patterns had a lower intensity.

All five phases exhibited distinctive high-intensity diffraction peaks and low total diffraction peaks, making their identification definitive, since they were mostly detected in the calculated diffraction patterns. Additionally, the simulated diffraction patterns of each mineralogical phase differ strongly from each other, which is why the matching of the mineralogical phases to the samples was apparent.

A detailed discussion of the identified phases follows, in alphabetical order.

4.1.2.1 Al

Al was identified based on its distinctive diffraction peak at approximately 38.5 ° and other supporting diffraction peaks, suggesting the presence of cubic Al (space group $Fm\bar{3}m$).

As mentioned in Subchapter 4.1.1, the Al present in the samples likely stems from the current collectors and cell casing. Based on the assumption that the samples were previously thermally treated, it is possible for Al to remain as an impurity in the active material. As studies have shown, the separation of the active material from Al current collector layers is largely possible with thermal treatments (Li & Zhu, 2024; Lombardo et al., 2021). Despite this, complete removal of Al is challenging due to its melting point at 660.3 °C, potentially leading to Al particles partially or entirely melting during the thermal treatment. This would lead to Al particles covering the active material particles, inhibiting the complete removal of Al from the active material (Li & Zhu, 2024; Lombardo et al., 2021; Y. Yang et al., 2016). When taking the elemental composition resulting from the XRD and SEM-EDS analysis into account, the relatively high proportion of Al could be an indication of the partial melting of Al particles during the thermal treatment. This reinforces the assumption that the samples were thermally treated

4.1.2.2 Graphite (C)

Graphite was identified by its distinctive diffraction peak at approximately 26.5 °, consistently detectable across measurements. When taking a closer look at Feed 1 in Figure 11, it is noticeable that the software assigned Graphite to the diffraction peak at 44.4 °, the same diffraction peak that was assigned to Ni. Compared to the other diffraction patterns, Graphite was assigned to the diffraction peak right to it at 44.6 °. While the difference in the 2θ angles is marginal, the intensity differs greatly from 774 counts to 165 counts for the diffraction peaks at 44.4 ° and 44.6 °, respectively. The inconsistent assigning of the mineralogical phases to the diffraction peaks would explain the lower Graphite content in Feed 1 compared to Feed 2 and 3.

The presence of Graphite, which facilitates Li^+ ion intercalation and deintercalation, is consistent with the LIB composition. When taking the assumed thermal treatment into account, studies have proven, that Graphite can withstand thermal treatments up to 600 °C, thus confirming its presence regardless of thermal treatments (Nam et al., 2009).

4.1.2.3 CoO, MnO, and Ni

The phases CoO, MnO, and metallic Ni were identified by their distinctive diffraction peaks at 42.4 °, 40.7 ° and 44.4 °, respectively, indicating their presence in all measurements. Since the calculated diffraction peaks at these angles were consistently

detected, as well as the other expected diffraction peaks, it can be assumed with absolute certainty that CoO, MnO and metallic Ni were present in the samples.

When discussing the origins of the mineralogical phases, CoO, MnO and metallic Ni, the crystal structure in which these phases are present needs to be examined. During thermal treatments, $NiMnCoO_x$ decomposes, thus reduced, to the respective metal oxides while undergoing phase transitions from an initially layered structure ($R\bar{3}m$) to a disordered spinel structure ($Fd\bar{3}m$), and at sufficiently high temperatures, to a rock-salt structure ($Fm\bar{3}m$) (Bak et al., 2014; Nam et al., 2009; Y. Yang et al., 2016). In the case of charged cathode material, where the transition metals have a high oxidation state, the temperature at which phase transitions occur is significantly influenced by the Ni concentration in cathode materials. The phase transition is particularly noticeable with Ni, as it is the least stable element in comparison to Co and Mn, and its reduction from higher to lower oxidation states happens the fastest during thermal treatments (Bak et al., 2014; Nam et al., 2009). Different compositions of NMC cathode materials exhibit distinct phase transition behaviors (Bak et al., 2014):

- NMC433: The transition from a layered to spinel structure begins at 250 °C, with no subsequent transition into a rock-salt structure.
- NMC532: The transition from a layered to spinel structure starts at 235 °C, without a transition into the rock-salt structure.
- NMC622: The transition from a layered to spinel structure initiates at 185 °C, followed by a transition from spinel to a rock-salt structure at 550 °C.
- NMC811: The transition from a layered to spinel structure starts at 135 °C, progresses to spinel to rock-salt structure at 350 °C, and partially transitions to metallic Ni at temperatures up to 600 °C.

Given this information, and the presence of CoO, MnO, and metallic Ni in the rock-salt structure (space group $Fm\bar{3}m$), it can be validated that the samples underwent thermal treatment. The temperature at which this process was performed is assumed to be approximately 600 °C for an extended period, considering that only metallic Ni was present in the samples. However, if discharged cathode material, thus with a lower oxidation state, was present in the active material, the temperature is believed to be lower than 600 °C. This cannot be validated nor rejected as the research studies in this field is scarce and no information is provided on the pretreatment steps on the active material used in this study.

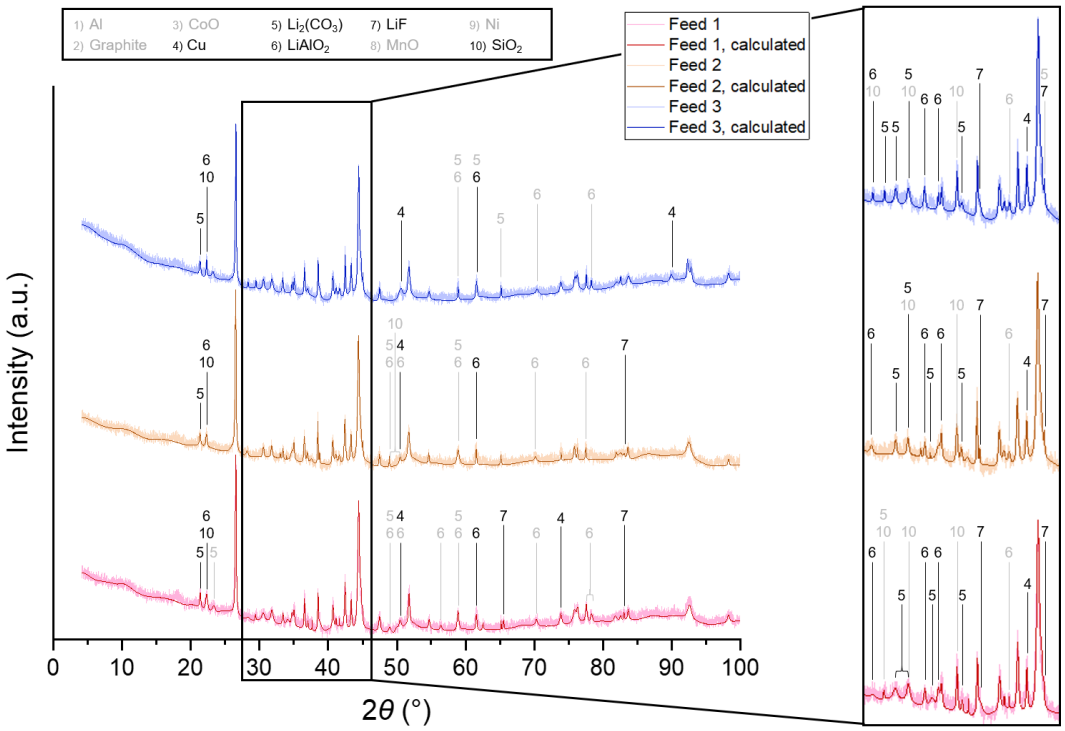

Figure 12 - Measured diffraction pattern of active material; Magnified view of diffraction pattern from 28 ° to 46 ° (right)

In Figure 12, the remaining mineralogical phases identified were Cu, $Li_2(CO_3)$, $LiAlO_2$, LiF and SiO_2. Based on the FoM provided by the software, Cu, LiF and SiO_2 were assigned next. The simulated diffraction patterns of Cu and LiF exhibited one distinctive high-intensity peak and a few lower-intensity peaks. However, due to the lower intensity of the calculated diffraction peaks compared to those of Al, Graphite, CoO, MnO, and Ni, matching Cu and LiF was less intuitive. The simulated diffraction patterns of SiO_2, on the other hand, exhibited one distinctive high intensity diffraction peak and several low intensity peaks. While the distinctive diffraction peak was identified in the calculated diffraction patterns, the remaining diffraction peaks were not always assigned.

Lastly, the mineralogical phases $Li_2(CO_3)$ and $LiAlO_2$ were matched to the samples by manually adding them to the selection procedure. The simulated diffraction patterns of both phases presented multiple high intensity diffraction peaks and many low intensity diffraction peaks. However, the distinctive diffraction peaks of both phases were assigned to low intensity diffraction peaks, while the remaining diffraction peaks of both phases were barely visible or not detectable. Consequently, the software was unable to identify these mineralogical phases during the automatic matching procedure.

A detailed discussion of the identified phases follows, in alphabetical order.

4.1.2.4 Cu

Cu was identified based on its distinctive diffraction peak at approximately 43.3 °, as well as on the remaining diffraction peaks. Considering that the simulated diffraction pattern of Cu had 5 diffraction peaks up to 100 °, the matching of Cu was just as clear and definitive as the matching of the mineralogical phases present in Figure 12. However, the assigned diffraction peaks were low in intensity, suggesting Cu being present in trace amounts. This coincides with the results on the composition of the XRD and SEM-EDS analysis.

Cu with a cubic crystal structure (space group $Fm\bar{3}m$) likely originates from anodic current collectors that were not removed prior to thermal treatment (Bhar et al., 2023). The low Cu content can be explained by the higher melting point of Cu at 1,085 °C, compared to Al. If the samples were treated at 500 – 600 °C, the Cu current collector would not partially melt, as it would with Al. The low Cu content therefore indicates that the samples were thermally treated at temperature below its melting point.

4.1.2.5 $Li_2(CO_3)$

$Li_2(CO_3)$ was identified by the multiple high intensity diffraction peaks between approximately 29.5 ° and 34.1 °, while the remaining simulated diffraction peaks of $Li_2(CO_3)$ were barely visible or not detected in the calculated diffraction patterns. Nonetheless, since all the distinctive high intensity diffraction peaks were identified in the calculated diffraction patterns, the $Li_2(CO_3)$ concentration in the samples is accordingly moderately high compared to other mineralogical phases presented in Figure 12.

Its presence, in a monoclinic crystal structure (space group C 1 2/c 1), suggests the decomposition of anode and cathode material to $Li_2(CO_3)$ and metal oxides during thermal treatments at 800 °C. Additionally, during roasting procedures at 650 °C in the presence of air and oxygen, the NMC active material decomposes to $Li_2(CO_3)$ and metal oxides, too (Makuza et al., 2021; Stallmeister & Friedrich, 2023). Thus, the presence of $Li_2(CO_3)$ further validates the hypothesis that the active material was previously thermally treated.

4.1.2.6 $LiAlO_2$

Among the phases identified, $LiAlO_2$ stands out due to the multiple high intensity diffraction peaks and few diffraction peaks with low intensities. During the matching process, almost all diffraction peaks of $LiAlO_2$ were identified in the calculated diffraction patterns. However, the assigned diffraction peaks were low in intensity, suggesting $LiAlO_2$ being moderately present in the samples.

The presence of $LiAlO_2$, with a tetragonal crystal structure (space group P 41 21 2), likely results from the reaction of Al with LiO_2 during thermal treatments. The cathode material

decomposes to LiO_2 during thermal treatments, before mineralogical phases such as $Li_2(CO_3)$ form. Thus, in the presence of Al, it is assumed that Al and LiO_2 leads to the formation of $LiAlO_2$ (Huang et al., 2021). Considering the scarce literature on the characterization of active material after thermal treatment, this assumption cannot be further validated or rejected.

4.1.2.7 LiF

LiF was identified by its distinctive diffraction peak at approximately 45.0 °, which was present in all measurements. The remaining low intensity diffraction peaks were not always present or identified in the calculated diffraction patterns, since the intensities were usually very low. Although the simulated diffraction peaks of LiF were present in the calculated diffraction patterns, the software did not always assign LiF to those diffraction peaks.

The presence of LiF with a cubic crystal structure (space group $Fm\bar{3}m$) presumably results from the decomposition of $LiPF_6$ electrolyte and PVDF binder during thermal treatments at 500 – 600 °C. $LiPF_6$ remains thermally stable up to 107 °C in a dry inert atmosphere (H. Yang et al., 2006). Considering that the samples were thermally treated at 500 – 600 °C, the electrolyte decomposes into LiF as a solid and PF_5 as a gas (Kriston et al., 2019). The decomposition of PVDF occurs at temperatures between 500 – 600 °C and produces fluoride-containing gases like HF, fluorinated hydrocarbons and other gases. The products, especially HF, are likely to form LiF during decomposition.

4.1.2.8 SiO_2

SiO_2 was identified by its distinctive diffraction peak at approximately 22.4 ° and assigned to a diffraction peak with low intensity. As with the other mineralogical phases discussed in Figure 12, the remaining simulated diffraction peaks of SiO_2 were either barely visible or not detected in the calculated diffraction patterns, as highlighted in grey in Figure 12.

The presence of SiO_2, identified as cristobalite in a tetragonal crystal structure (space group P 41 21 2), likely originates from the surface coatings of the cathode material. The oxide-based coating inhibits the direct contact of the cathode material with the electrolyte, which would decrease the battery performance over time (Malik et al., 2022). Metal oxides, including SiO_2, are commonly used on an industrial scale as surface coating in NMC cathode materials.

In conclusion, the XRD analysis provides critical insights into the mineralogical phases present in the active material, confirming the presence of key components and suggesting thermal treatment history. Further detailed analysis with XRD and other methods will enhance the understanding of these phases and their implications for material processing and recycling.

4.1.3 Comparison of Chemical Composition Results of XRD and SEM-EDS Analysis

Having established the XRD results, a comparison with the SEM-EDS results is necessary. For this purpose, the elements relevant to the active material and measured in both analyses, specifically Al, C, Co, Cu, Mn, Ni, O, and Si, are analyzed in more detail. In Table 5, the chemical composition results from both XRD and SEM-EDS analyses are compared using percentage deviation.

Element	Chemical Composition (%)		Percentage Deviation (%)
	SEM-EDS	XRD	SEM-EDS to XRD
Al	3.47	7.87	- 126.80
C	60.17	50.20	16.57
Co	5.83	3.07	47.34
Cu	0.40	1.53	- 282.50
Mn	1.73	2.43	-40.46
Ni	1.63	9.13	- 460.12
O	25.6	15.10	41.02
Si	0.4	0.83	- 107.50

Table 5 – Comparison of chemical composition results of SEM-EDS and XRD

C was the only element for which the chemical composition did not differ greatly between the two analyses, with a percentage deviation of approximately 17 %. The largest differences in chemical composition were observed for Cu and Ni, with percentage deviations of approximately 282 % and 460 %, respectively. For the remaining elements, including Al, Co, Mn, O, and Si, the percentage deviation ranged between approximately 40 % and 127 %, which is still a significant difference.

It should be noted that SEM-EDS analysis measures the surface of the samples, while XRD analysis penetrates deeper into the sample. Therefore, the chemical composition results from SEM-EDS varied significantly from those of XRD. This discrepancy is likely because finer particles, such as Ni, may be located below the surface measured by SEM-EDS and thus were not detected.

4.1.4 Conclusion to RQ 1

Concluding the XRD and SEM-EDS analysis of the NMC active material, the main RQ of this study can be answered: whether active material can be properly characterized using these methods. Both analytical methods confirmed the presence of certain elements in the samples, specifically Al, C, Co, Cu, Mn, Ni, O, and Si. Additionally, literature research

prompted the inclusion of elements such as F and Li in the XRD analysis to identify all mineralogical phases in the samples, while elements like Ca, Cl, Mg, and S were excluded due to their unexpected presence in the active material.

The elemental mapping from SEM-EDS analysis largely corroborated the mineralogical phases identified by XRD analysis. Based on the mineralogical phases found, assumptions were made regarding possible pretreatments of the active material. It was confirmed that the samples originated from LIBs with Graphite and NMC-based anode and cathode materials, respectively. The presence of Al and Cu suggested mechanical treatments of battery cells, where current collector foils were not removed. The detection of CoO, MnO, and metallic Ni strongly indicated thermal treatment of the samples between 550 – 600 °C. This assumption was further supported by the presence of Al, Cu, CoO, MnO, $LiAlO_2$, $Li_2(CO_3)$, and LiF. Furthermore, the thermal decomposition of $NiMnCoO_x$ leads to the release of O, explaining the high O content measured in the SEM-EDS analysis.

As anticipated, the XRD analysis of the feed material produced diffraction patterns with numerous peaks and a high background signal, resulting from the many phases present in the active material. Additionally, it is believed that amorphous materials, distorted crystal structures and the orientation of phases, such as Graphite, negatively affect the diffraction patterns. Thus, the identification of mineralogical phases and determination of the mineralogical composition was challenging.

Therefore, froth flotation was applied to separate Graphite and other hydrophobic phases from the remaining phases, aiming to obtain clearer XRD analysis results. The subsequent chapters will present and discuss the process of simulated froth flotation and the resulting XRD analysis of the froth flotation products.

4.2 Simulated Froth Flotation

The froth and pulp products resulting from the froth flotation process carried out in a self-built flotation cell are briefly described in this chapter. During the simulated froth flotation, a stable froth layer containing many air bubbles with attached particles was observed. The process was concluded after 15 minutes when the froth layer decreased, and the air bubbles carried fewer particles. The following Figure 13 shows the simulated froth flotation process.

Figure 13 - Simulated froth flotation process

Upon transferring the froth and pulp products into separate beakers, it was noticeable that most of the material in the froth products floated on the surface, while the material in the pulp products sank to the bottom, as shown in Figure 14.

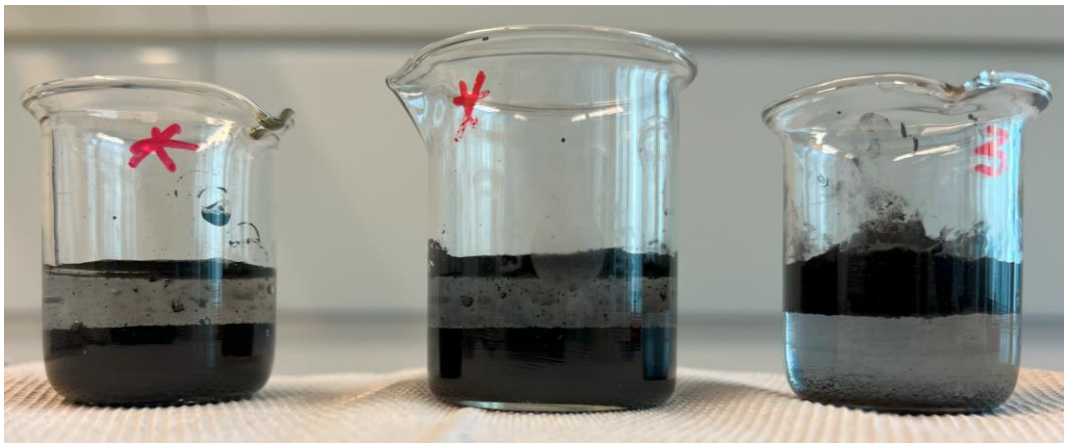

Figure 14 – Pulp products in the left and middle beaker; Froth product in the right beaker

After drying, there was a distinguishable difference in texture and color between the froth and pulp products. The froth product had a rougher texture, particularly noticeable during mortaring, whereas the pulp product was softer and broke easily when mortared. Some shiny particles were present in the froth product, while the pulp product was predominantly black, in contrast to the dark grey froth product, as presented in Figure 15a and 15b. Additionally, a white-greyish residue was found on the rims of the beakers where the pulp products were stored. This residue fell off in flakes when scraped, as shown in Figure 15c and 15d.

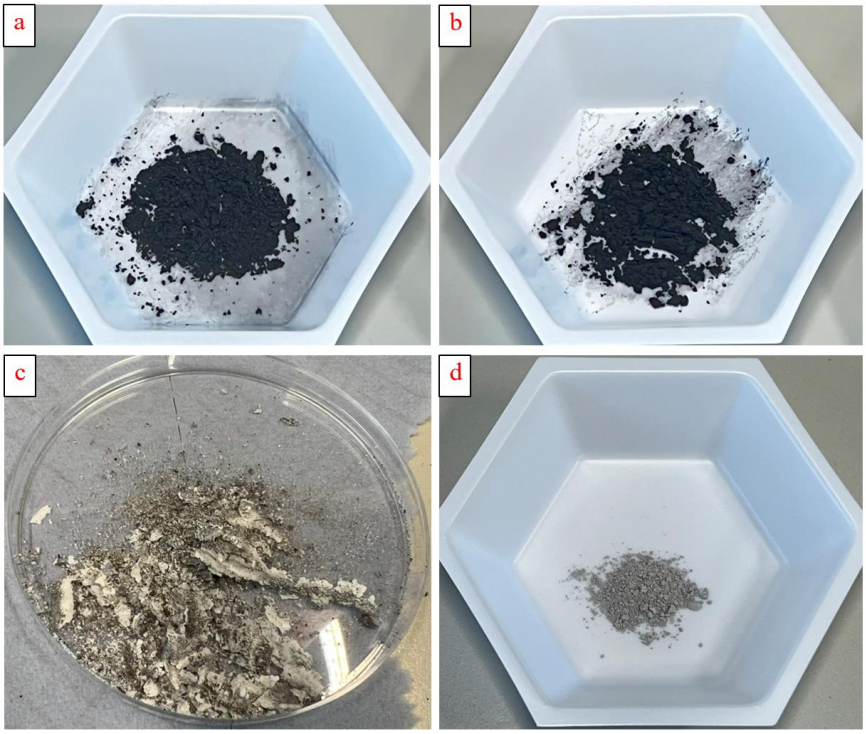

Figure 15 – Froth product (a) and pulp product (b); White residue from Pulp Product 1 before (c) and after mortaring (d)

4.3 XRD Characterization of NMC Active Material after the Simulated Froth Flotation

During the simulated froth flotation process, the feed material was separated into two fractions: froth and pulp product. The mineralogical composition of these fractions will be discussed in the following subchapters. The average mineralogical compositions of the froth and pulp product samples are displayed in Tables 6 and 8, respectively. The diffraction patterns of the froth and pulp product samples are presented in Figures 16 and 17, respectively. Additionally, white residues formed during the drying process of the pulp products were individually analyzed by XRD, as shown in Figure 18.

4.3.1 Froth Product

Phase	Formula	Mineralogical Composition (%)				Mean value	Standard deviation
Froth Product Samples		1	2	3	4		
Aluminum	Al	0.30	0.40	3.00	1.30	1.25	1.08
Graphite	C	66.10	62.00	56.20	52.50	59.20	5.23
Copper (II) oxide	CoO	4.30	5.20	8.30	4.70	5.63	1.58
Copper	Cu	0.70	0.50	0.70	1.50	0.85	0.38
Zabuyelite	$Li_2(CO_3)$	15.90	17.80	7.80	12.40	13.48	3.81
Lithium aluminum oxide	$LiAlO_2$	0.50	0.20	2.00	9.60	3.08	3.83
Lithium fluoride	LiF	3.30	4.00	3.30	3.50	3.53	0.29
Manganosite	MnO	2.00	2.10	3.70	2.30	2.53	0.69
Nickel	Ni	2.90	5.30	12.90	9.10	7.55	3.80
Cristobalite	SiO_2	4.00	2.50	2.10	3.30	2.98	0.73

Table 6 – Mineralogical phase composition of froth product from XRD analysis

Phase	Formula	Mean value	Standard deviation	Feed material mean value	Change (%)
Aluminum	Al	1.25	1.08	4.97	- 74.85
Graphite	C	59.20	5.23	48.00	23.33
Copper (II) oxide	CoO	5.63	1.58	3.93	43.13
Copper	Cu	0.85	0.38	1.53	- 44.44
Zabuyelite	$Li_2(CO_3)$	13.48	3.81	14.10	- 4.43
Lithium aluminum oxide	$LiAlO_2$	3.08	3.83	7.13	- 56.87
Lithium fluoride	LiF	3.53	0.29	6.53	- 46.02
Manganosite	MnO	2.53	0.69	3.13	- 19.33
Nickel	Ni	7.55	3.80	9.03	- 16.39
Cristobalite	SiO_2	2.98	0.73	1.80	65.28

Table 7 – Comparison of phase composition of froth product and feed material

The XRD analysis of the froth product samples showed an increase in Graphite, CoO and SiO_2 content compared to the feed material, as indicated in green in Table 7. In contrast, the content of Al, Cu, $LiAlO_2$ and LiF decreased significantly, marked in orange in Table

7. The proportions of $Li_2(CO_3)$, MnO and Ni showed less than 20 % change, indicating a slight decrease in their concentration.

Regarding the diffraction patterns, the order of matching mineralogical phases affected the phase composition. While the diffraction patterns will not be discussed in as much detail as previously done for the feed material, notable abnormalities or differences will be mentioned.

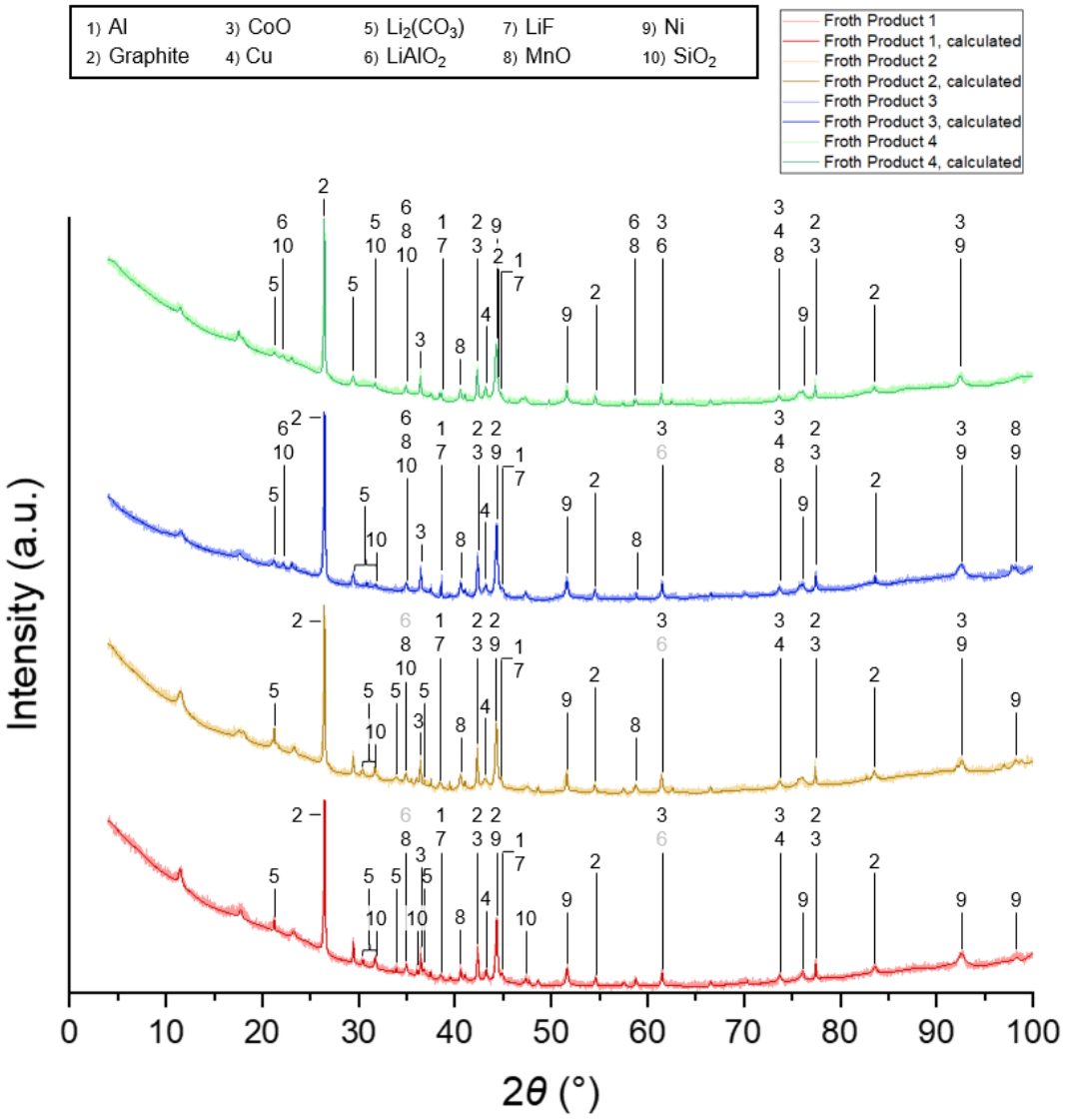

Figure 16 – Measured diffraction pattern of froth product samples

At first glance, the calculated diffraction patterns differed slightly in their intensities, especially between approximately 29 ° and 45 °, despite all originating from the froth product. The remaining diffraction peaks in all four samples were relatively consistent, with minor differences in their intensities. Notably, two new diffraction peaks appeared at approximately 11.5° and 17.7°.

The highest intensity diffraction peaks remained at approximately 26.4 °, 36.4 °, 42.4 °, and 44.3 °, similar to the feed material. Based on these high-intensity diffraction peaks,

CoO, Graphite, and Ni were assigned to the calculated diffraction patterns. In contrast to the feed material, MnO was identified based on the FoM provided, as the corresponding diffraction peaks in the measurements were lower in intensity compared to the feed material. Despite this, the simulated diffraction peaks of all four phases were identified in the calculated diffraction patterns of the froth product.

SiO_2 and $Li_2(CO_3)$ were also identified based on the FoM provided. The distinctive diffraction peak of SiO_2 at approximately 22.5 ° was detected in three of the four measurements, though it was assigned to a low-intensity peak. Although $Li_2(CO_3)$ was detected, its high-intensity distinctive diffraction peaks were either barely visible or not visible in the calculated diffraction patterns. However, since most of the diffraction peaks of $Li_2(CO_3)$ were present, it is speculated that the automatic matching program assigned $Li_2(CO_3)$ to the samples on this basis.

The remaining mineralogical phases, Al, Cu, $LiAlO_2$ and LiF, had to be manually added to the selection process. The distinctive diffraction peaks for these phases were identified in the calculated diffraction patterns, although they were either very low in intensity or had already been assigned to another mineralogical phase. As mentioned in Subchapter 3.1.2.2, the matching program subtracts the intensity of the already assigned diffraction peak, thus tends to exclude these diffraction peaks when assigning new phases. Therefore, these phases had to be added manually to the selection process. By comparing the simulated with the calculated diffraction patterns, the distinctive diffraction peaks with high intensities were almost always identified in the calculated diffraction patterns as low-intensity diffraction peaks.

4.3.2 Pulp Product

Phase	Formula	Mineralogical Composition (%)				Mean value	Standard deviation
Pulp Product Samples		1	2	3	4		
Aluminum	Al	1.40	3.90	2.20	1.30	2.20	1.04
Graphite	C	58.30	64.40	42.20	49.80	53.68	8.41
Copper (II) oxide	CoO	5.20	5.30	5.20	7.00	5.68	0.77
Copper	Cu	1.10	1.10	1.00	0.90	1.03	0.08
Zabuyelite	$Li_2(CO_3)$	8.00	10.60	25.70	22.80	16.78	7.60
Lithium aluminum oxide	$LiAlO_2$	4.50	1.20	6.30	4.70	4.18	1.85
Lithium fluoride	LiF	5.80	2.80	5.50	0.60	3.68	2.13
Manganosite	MnO	3.00	1.10	2.20	1.50	1.95	0.72
Nickel	Ni	11.40	8.70	8.00	10.30	9.60	1.33
Cristobalite	SiO_2	1.40	0.80	1.70	1.10	1.25	0.34

Table 8 – Mineralogical phase composition of pulp product from XRD analysis

Phase	Formula	Mean value	Standard deviation	Feed material mean value	Change (%)
Aluminum	Al	2.20	1.04	4.97	-55.73
Graphite	C	53.68	8.41	48.00	11.82
Copper (II) oxide	CoO	5.68	0.77	3.93	44.40
Copper	Cu	1.03	0.08	1.53	-33.01
Zabuyelite	$Li_2(CO_3)$	16.78	7.60	14.10	18.97
Lithium aluminum oxide	$LiAlO_2$	4.18	1.85	7.13	-41.44
Lithium fluoride	LiF	3.68	2.13	6.53	-43.72
Manganosite	MnO	1.95	0.72	3.13	-37.70
Nickel	Ni	9.60	1.33	9.03	6.31
Cristobalite	SiO_2	1.25	0.34	1.80	-30.56

Table 9 – Comparison of phase composition of pulp product and feed material

The XRD analysis of the pulp product samples indicated a significant increase in $Li_2(CO_3)$, and CoO content, while the Graphite and Ni concentration increased by 11.82 % and 6.31 %, respectively, as highlighted in green in Table 9. The content of the remaining phases,

Al, Cu, $LiAlO_2$, LiF, MnO, and SiO_2, decreased significantly with changes over 30 %, marked in orange in Table 9.

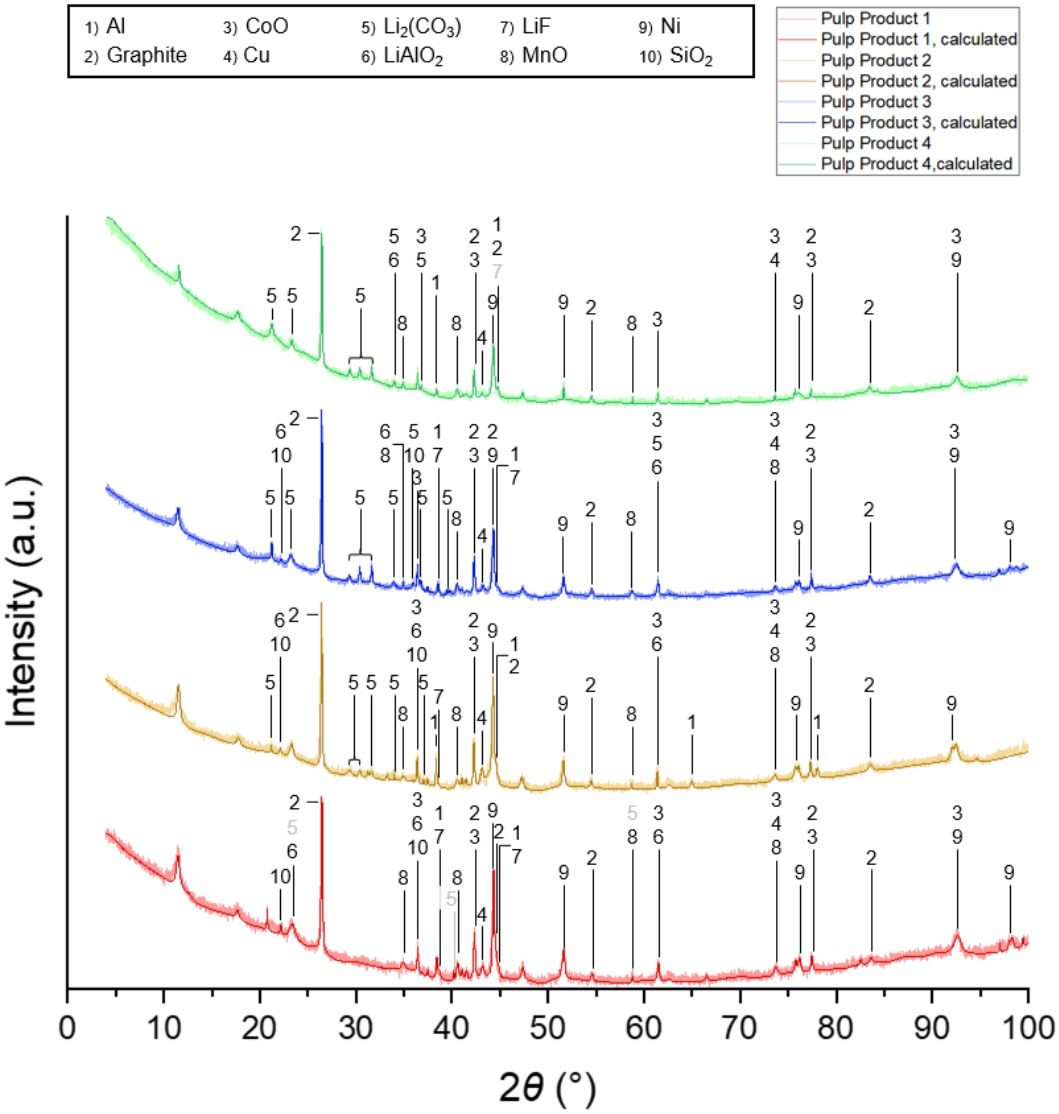

Figure 17 – Measured diffraction pattern of pulp product samples

Similar to the froth product, the calculated diffraction patterns of the pulp product showed variations between approximately 26 ° and 44 °. The same two new diffraction peaks observed in the froth product at approximately 11.5 ° and 17.7 ° were also present in the pulp product. Compared to the froth product, the diffraction peak at 11.5° had a higher intensity. Additionally, the diffraction peaks measured from 50 ° onward were relatively higher in intensity than those in the froth product. Notably, the diffraction peaks at approximately 44.3 ° and 51.6 ° were significantly higher in intensity, particularly in Pulp Product 1 and 2.

During the matching of mineralogical phases of the pulp product, CoO, Graphite, and Ni were assigned to the calculated diffraction patterns based on the measured high intensity diffraction peaks at approximately at 26.4 °, 42.3 ° and 44.3 °. The distinctive diffraction

peak of Ni, along with its remaining peaks, had higher intensity compared to those in the froth product, consistent with the higher Ni content in the pulp product as shown in Table 8.

MnO and $Li_2(CO_3)$ were assigned based on the FoM provided. Compared to the feed material, the distinctive peak of MnO at approximately 40.6 ° was significantly lower in intensity, justifying the matching of MnO by the FoM provided. As in the froth product, $Li_2(CO_3)$ was assigned to the calculated diffraction patterns because most of its diffraction peaks were identified. Its distinctive diffraction peaks between 29 ° and 32 ° were more pronounced compared to the froth product, except in Pulp Product 1, where these peaks did not appear due to the missing presence of white residues, later identified as $Li_2(CO_3)$, explaining the missing peaks. The diffraction pattern of the white residue will be discussed with Figure 18.

The remaining mineralogical phases, Al, Cu, $LiAlO_2$, LiF and SiO_2, were manually added to the selection process. Although the distinctive diffraction peak of Al at approximately 38.5 ° was more visible in the diffraction patterns compared to the froth product, the remaining diffraction peaks of Al were not detected in the pulp product measurements. This would explain why Al was not automatically detected by the matching program. The same observation applied to Cu, $LiAlO_2$ and SiO_2.

For the diffraction patterns of the froth flotation products, matching the mineralogical phases to the diffraction patterns was easier compared to the feed material. This is because the diffraction peaks in the froth flotation product measurements were more clearly distinguishable from each other, with less overlapping diffraction peaks compared to the feed material. Although the intensities of the diffraction peaks in the froth flotation products were weaker than in the feed material, the matching program automatically identified phases like $Li_2(CO_3)$ for example, which had to be manually added to the feed products.

It is crucial to mention that all mineralogical phases present in the feed material were included during the characterization of both froth and pulp products, even when the distinctive diffraction peaks were not clearly identified in the calculated diffraction patterns. The rationale behind this was to provide a holistic comparison between the composition of the active material before and after the simulated froth flotation process. Since the simulated froth flotation separated the feed material into two products, the concentration of certain mineralogical phases, such as $LiAlO_2$ and LiF, is believed to have naturally decreased in both products, influencing the intensities of the diffraction peaks. Additionally, it is believed that some mineralogical phases, such as $LiAlO_2$ and LiF, dissolved during the froth flotation process, leading to the decreased concentration in both products. However, further research needs to be conducted to analyze these behaviors.

As mentioned in Subchapter 3.1.2.2, when adjusting the baseline, it is assumed that diffraction peaks with low intensities were easily obscured by the high background signals, which may have resulted in these diffraction peaks not being identified during the search for diffraction peaks.

4.3.3 XRD Characterization of White Residues from the Pulp Product

Lastly, the XRD characterization of the white residue found on the rim of the beakers in which Pulp Product 1 was dried is presented. At first glance, it is noticeable that the diffraction pattern showed clearer and narrower diffraction peaks with reduced background signals compared to the feed, froth, and pulp products. These features suggest that the white residue contained fewer phases.

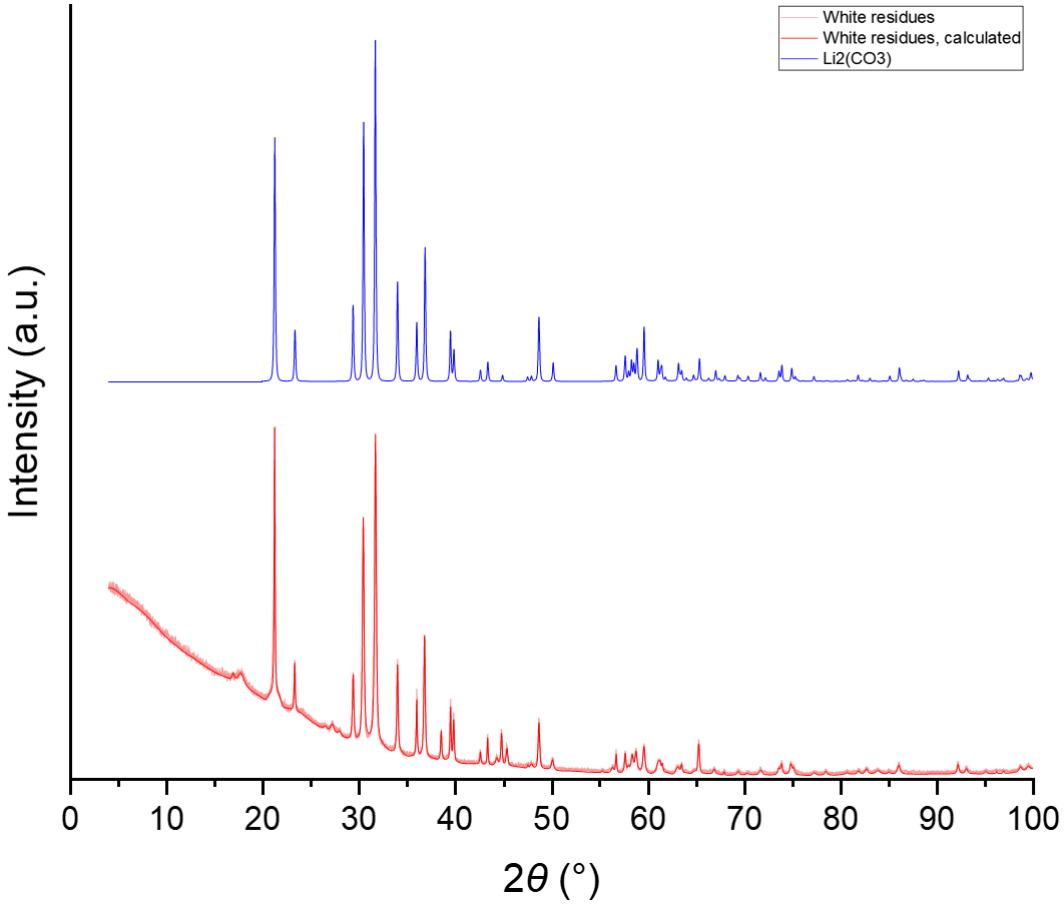

Figure 18 – Measured diffraction pattern of white residues (red); Simulated diffraction pattern of $Li_2(CO_3)$ (blue)

The automatic matching program identified this sample as $Li_2(CO_3)$. This result was confirmed manually by comparing the simulated diffraction pattern of $Li_2(CO_3)$ with the calculated diffraction pattern. verifying that the white residue was indeed $Li_2(CO_3)$. A slight Al impurity was detected, with a concentration below 2 %.

Regarding the origin of the highly concentrated $Li_2(CO_3)$ in the white residues from Pulp Product 1, it is assumed that during the drying process, $Li_2(CO_3)$ was primarily present on

the water surface and adhered to the rim of the beaker as the water evaporated. However, since $Li_2(CO_3)$ was still present in Pulp Product 1 in lower concentrations compared to the other products, this assumption might not fully explain the behavior. No further analysis was conducted to clarify this result, and existing literature does not provide an explanation for this phenomenon.

Nevertheless, this result confirms with absolute certainty that $Li_2(CO_3)$ is present in the samples.

4.3.4 Conclusion to RQ 2

Having presented the results of the XRD characterization of both froth flotation products, the outcomes will now be discussed in relation to the RQ of this study.

To address the RQ of whether the simulated froth flotation improved the characterization of NMC active material by XRD, a comparison of the diffraction patterns of the feed material, froth, and pulp products is necessary. From here on, the froth and pulp products will be collectively referred to as froth flotation products, excluding the white residue.

At first glance, the feed material exhibited a higher number of diffraction peaks compared to the froth flotation products. However, the diffraction patterns of the froth flotation products were clearer and easier to analyze because the diffraction peaks did not overlap as much, allowing multiple phases to be assigned to staggered diffraction peaks. An excellent example is the automatic matching of $Li_2(CO_3)$ to the froth flotation products, illustrating the differences in diffraction patterns and the challenges in matching mineralogical phases to the feed material.

A closer examination of the background signal reveals that the froth flotation products had a lower background signal, indicating fewer mineralogical phases present in the sample. Nonetheless, the background signal in the diffraction patterns of the froth flotation products remained high compared to the nearly single-phase composition of the white residue, which is primarily $Li_2(CO_3)$.

In conclusion, the simulated froth flotation process evidently improved the XRD characterization of the NMC active material. By utilizing froth flotation, the froth and pulp products contained fewer mineralogical phases, thus providing a clearer and more precise XRD analysis.

4.3.5 Conclusion to RQ 3

Lastly, to answer the RQ on how efficiently the simulated froth flotation separated the NMC active material, the mineralogical composition of the froth and pulp products needs to be examined more closely. It is important to consider that froth flotation was applied in

this study as a basic assessment of whether the fundamental principle of hydrophobic differences can be utilized to separate the active material prior to the recovery of individual materials in subsequent recycling processes. Therefore, the results can only be used for a rough evaluation of the efficiency of froth flotation and should not be used as comparative data.

The main mineralogical phases evaluated for froth flotation efficiency in this study were Graphite and Ni. Graphite content increased by approximately 23 % in the froth product and 12 % in the pulp product, with a more significant increase in the froth product. However, when taking a closer look at the individual froth and pulp product samples, the Graphite content generally decreased in the pulp product samples, except for Pulp Product 2, and increased significantly in the froth product samples, except for Froth Product 4. The increase of Graphite content in the froth products is coincides with the results found in the literature (Vanderbruggen et al., 2021; G. Zhang et al., 2018).

Ni concentration decreased in the froth product and increased slightly in the pulp product, consistent with literature, indicating successful separation from Graphite (Vanderbruggen et al., 2021; G. Zhang et al., 2018). Ni and other transitional metal oxides are expected to be concentrated in the pulp products due to their more prominent hydrophilic properties compared to Graphite (Vanderbruggen et al., 2021). However, due to the turbulence in the flotation cell, caused by the airflow and stirring, Ni particles might have been pushed towards the surface while the froth was collected. Furthermore, considering that a magnetic stirrer was used, the adhering particles on the magnetic stirring sticks are believed to be Ni and Co. Since the magnetic stirring sticks were removed and cleaned separately, an unknown amount of Ni could have been removed and thus negatively influenced the Ni concentration in the pulp product.

Combining the slight increase in Graphite content in the pulp product and the small decrease of Ni concentration in the froth product, it is likely that the collection method used influenced the results by inadvertently including Graphite in the pulp product and Ni in the froth product. Since the froth flotation process and the collection of the products were not done with the proper equipment, it is believed that when transferring the remaining products after the froth was removed, the remaining Graphite on the walls of the flotation cell was transferred with the pulp product into the beakers used for drying. With Ni, it is believed that some particles were unintentionally collected while scrapping off the froth layer. Nonetheless, based on the increase and decrease in Graphite and Ni content in the froth flotation products, respectively, it can be said that the simulated froth flotation process did indeed separate Graphite from Ni in the active material to some extent.

Other mineralogical phases, such as CoO and MnO, showed mixed results. CoO increased in both flotation products, while MnO decreased in both froth and pulp products, suggesting incomplete separation. As previously mentioned, it is expected for the transitional metal oxides to be concentrated in the pulp product due to their hydrophilicity (Vanderbruggen et al., 2021). While the increase of CoO concentration in the pulp product and the decrease of MnO content in the froth product are good indicators for a successful separation of active material, the contrasting results of CoO and MnO concentrations suggest otherwise. It is believed that the improper collection of the froth product has also led to CoO particles being unintentionally collected with the froth layer. However, for the remaining results no assumptions can be made since the reason behind these results are unclear and requires further analysis or another cycle of froth flotation to examine these outcomes.

Li compounds, such as $Li_2(CO_3)$, $LiAlO_2$ and LiF, significantly decreased in the froth product. However, the $LiAlO_2$ and LiF concentrations also significantly decreased in the pulp product. The $Li_2(CO_3)$ concentration, on the other hand, increased in the pulp product, indicating it is not hydrophobic and can be separated from Graphite using froth flotation. The higher $Li_2(CO_3)$ content in the pulp product was also visible due to the white residues found mainly on the rims of the beaker in which the pulp product was dried in. Compared to the literature, the froth flotation process reported an increased Li concentration in the pulp products due to its hydrophilicity (Vanderbruggen et al., 2021). However, it is unclear in what mineralogical phase Li is present in the froth flotation processes found in the literature.

Current collector materials, Al and Cu, decreased equally in both froth and pulp products, indicating froth flotation is not effective for their separation. Their hydrophobicity appears to be intermediate compared to other materials studied. Thus, further research is required on the hydrophobic properties of Al and Cu.

The SiO_2 concentration increased significantly in the froth product and decreased in the pulp product, suggesting successful separation from hydrophilic materials. It also suggests that SiO_2 in form from cristobalite could be hydrophobic, however the hydrophobic properties of SiO_2 needs to be further investigated by analyzing its surface chemical properties.

In conclusion, based on the experimental results, froth flotation demonstrates potential for separating active materials into two more concentrated products, enhancing the efficiency of subsequent metallurgical recycling treatments. Graphite concentration significantly increased in froth products, while Ni concentration decreased, coinciding with literature and indicating effective separation. The varying results for CoO, MnO, and Li compounds suggest that further analysis or additional flotation cycles are needed to confirm separation

efficiency. The significant increase in SiO_2 concentration in froth products suggests successful separation of SiO_2 from hydrophilic materials. However, the process appears ineffective for separating Al and Cu from the active material. Additionally, the standard deviations indicate significant variations in the mineralogical content within each product. This is likely due to the use of a self-built flotation cell with common materials in the simulated froth flotation. Although the main principles of froth flotation, including airflow, agitation, and the utilization of reagents, were applied, the results should not be compared to those from laboratory froth flotation devices. Nonetheless, this study provides a guideline suggesting that froth flotation is a viable option for separating active materials.

5 Conclusion and Outlook

5.1 Conclusion

RQ 1: XRD and SEM-EDS characterization of SLIB active material with Graphite and NMC-based electrode materials

This study investigated the characterization of active material from SLIBs using XRD and SEM-EDS. The primary RQ focused on the effectiveness of XRD and SEM-EDS in characterizing the active material. The analyses confirmed the presence of elements such as Al, C, mainly present as Graphite, Co, Cu, Mn, Ni, O, and Si. These findings validated that the samples originated from Graphite and NMC-based electrode materials and had undergone mechanical and thermal treatment, as indicated by the presence of Al, Cu, and other elements.

The SEM-EDS analysis identified the elements present in the samples, which were used for XRD characterization. The individual particles of Al and Cu confirmed that current collectors were not removed prior to mechanical pretreatment. Li was not detected due to the limitations of standard SEM-EDS devices, which cannot detect the low-energy of the characteristic X-rays emitted by Li.

The XRD analysis indicated that the active material initially included Graphite and NMC-based electrode materials, current collector fractions, electrolyte, and organic binder. The presence of Al and Cu in various concentrations suggested that current collectors and cell structures were not removed beforehand, indicating the mechanical pretreatment of whole battery cell units. The identification of CoO, MnO, and metallic Ni confirmed thermal treatments at approximately 600 °C. Additionally, the presence of $Li_2(CO_3)$, $LiAlO_2$, and LiF validates the thermal treatment of the active material samples. The decomposition of electrolyte, organic binder, and cathode materials, and the presence of Al is believed to

have caused the formation of the mentioned Li compounds. The presence of cristobalite (SiO_2) indicates the use of surface coatings on the cathode materials.

RQ 2: Improved XRD Characterization After Froth Flotation

The second RQ examined whether the simulated froth flotation process would improve XRD characterization. The diffraction patterns of the froth flotation products were clearer and easier to analyze due to the reduced number of mineralogical phases, reducing the likelihood of overlapping and occluding diffraction peaks. Thus, by separating the active material into two more concentrated products, the XRD characterization of the active material was clearer.

RQ 3: Fundamental Separation Efficiency of Graphite and LMOs using Froth Flotation

The third RQ explored the fundamental efficiency of the froth flotation process. The results showed an increase in Graphite content in the froth product and a decrease in Ni concentration, indicating successful separation to some extent. The presence of $Li_2(CO_3)$ in the white residues found on the rims of the beaker after drying suggested successful separation of lithium mineralogical phases from the active material. However, varying concentrations of CoO, MnO, and Li compounds indicated that further research and multiple froth flotation cycles are necessary to achieve better separation. The separation of Al and Cu was ineffective, as their concentrations decreased in both froth and pulp products.

5.2 Outlook

Standard SEM-EDS devices currently lack the sensitivity to detect Li, which poses a limitation for comprehensive analysis of active materials from SLIBs. Future studies should employ more sensitive SEM-EDS devices capable of detecting Li to overcome this limitation.

Due to the multi-phased nature of active material, the potential presence of amorphous materials and destructed crystal structures, as well as the orientation of materials such as Graphite, it is insufficient to rely solely on XRD analysis for the characterization of active material. The resulting diffraction patterns are often difficult to interpret, and the identification of mineralogical phases becomes challenging. Hence, it is recommended to complement XRD with other analytical methods to achieve more accurate characterization.

The froth flotation process demonstrated partial success in separating Graphite and LMOs. However, further investigation is required to enhance the separation efficiency. Froth flotation holds promise as a viable technique for separating electrode materials before recycling individual phases for their reuse in new LIBs. Future research should focus on

applying multiple froth flotation cycles to improve separation efficiency. Additionally, identifying suitable reagents and determining their optimal conditioning time through analyzing the reagent adsorption on the active material will be crucial. Understanding the hydrophobic properties of the phases present in the active material is also essential for improving froth flotation separation.

Further research should be conducted on the components of active material after each recycling step, including the pretreatment stage. This approach will provide clarity on the mineralogical phases present at each stage, ultimately enhancing the recovery rate of these phases in subsequent recycling steps. By tailoring recycling methods based on the phases present, more efficient and effective recycling processes can be developed, contributing to the sustainability and circularity of LIB usage.

6 References

Bak, S.-M., Hu, E., Zhou, Y [Yongning], Yu, X [Xiqian], Senanayake, S. D., Cho, S.-J., Kim, K.-B., Chung, K. Y., Yang, X.-Q., & Nam, K.-W. (2014). Structural changes and thermal stability of charged LiNixMnyCozO₂ cathode materials studied by combined in situ time-resolved XRD and mass spectroscopy. *ACS Applied Materials & Interfaces*, *6*(24), 22594–22601. https://doi.org/10.1021/am506712c

Baum, Z. J., Bird, R. E., Yu, X [Xiang], & Ma, J. (2022). Lithium-Ion Battery Recycling─Overview of Techniques and Trends. *ACS Energy Letters*, *7*(2), 712–719. https://doi.org/10.1021/acsenergylett.1c02602

Bhar, M., Ghosh, S., Krishnamurthy, S., Kaliprasad, Y., & Martha, S. K. (2023). A review on spent lithium-ion battery recycling: from collection to black mass recovery. *RSC Sustainability*, *1*(5), 1150–1167. https://doi.org/10.1039/D3SU00086A

Brückner, L., Frank, J., & Elwert, T. (2020). Industrial Recycling of Lithium-Ion Batteries—A Critical Review of Metallurgical Process Routes. *Metals*, *10*(8), 1107. https://doi.org/10.3390/met10081107

Bunaciu, A. A., Udriştioiu, E. G., & Aboul-Enein, H. Y. (2015). X-ray diffraction: Instrumentation and applications. *Critical Reviews in Analytical Chemistry*, *45*(4), 289–299. https://doi.org/10.1080/10408347.2014.949616

Chauhan, A., & Chauhan, P. (2014). Powder XRD Technique and its Applications in Science and Technology. *Journal of Analytical & Bioanalytical Techniques*, *5*(6). https://doi.org/10.4172/2155-9872.1000212

Chernyaev, A., Kobets, A., Liivand, K., Tesfaye, F., Hannula, P.-M., Kallio, T., Hupa, L., & Lundström, M. (2024). Graphite recovery from waste Li-ion battery black mass for direct re-use. *Minerals Engineering*, *208*, 108587. https://doi.org/10.1016/j.mineng.2024.108587

DERA. (2021). *Batterierohstoffe für die Elektromobilität*. https://www.deutsche-rohstoffagentur.de/DERA/DE/Downloads/DERA%20Themenheft-01-21.html

Epp, J. (2016). X-ray diffraction (XRD) techniques for materials characterization. In *Materials Characterization Using Nondestructive Evaluation (NDE) Methods* (pp. 81–124). Elsevier. https://doi.org/10.1016/B978-0-08-100040-3.00004-3

European Commission, & Directorate General for Internal Market, Industry, Entrepreneurship and SMEs. (2023). *Study on the critical raw materials for the EU 2023: Final report*. Publications Office. https://doi.org/10.2873/725585

European Parliament. (2022). *New EU rules for more sustainable and ethical batteries | Topics | European Parliament*. https://www.europarl.europa.eu/topics/en/article/20220228STO24218/new-eu-rules-for-more-sustainable-and-ethical-batteries

European Parliament (2023). EU ban on sale of new petrol and diesel cars from 2035 explained | News | European Parliament. https://www.europarl.europa.eu/pdfs/news/expert/2022/11/story/20221019STO44572/20221019STO44572_en.pdf

Eva, M., Mihai, F.-C., & Munteanu, A.-V. Sustainability of the transport sector during the last 20 years: Evidences from a panel of 35 countries. In (pp. 687–694). MISC; Albena. https://www.ssoar.info/ssoar/handle/document/63544

Gaston, B., & Protter, C. (2019). Energy-Dispersive X-ray Spectroscopy (EDS). *Libretexts*. https://chem.libretexts.org/Courses/Franklin_and_Marshall_College/Introduction_to_Materials_Characterization__CHM_412_Collaborative_Text/Spectroscopy/Energy-Dispersive_X-ray_Spectroscopy_(EDS)

Girão, A. V., Caputo, G., & Ferro, M. C. (2017). Application of Scanning Electron Microscopy–Energy Dispersive X-Ray Spectroscopy (SEM-EDS). In *Comprehensive Analytical Chemistry. Characterization and Analysis of Microplastics* (Vol. 75, pp. 153–168). Elsevier. https://doi.org/10.1016/bs.coac.2016.10.002

Huang, Z., Qiu, R., Lin, K., Ruan, J., & Xu, Z. (2021). In Situ Recombination of Elements in Spent Lithium-Ion Batteries to Recover High-Value γ-LiAlO2 and LiAl5O8. *Environmental Science & Technology*, *55*(11), 7643–7653. https://doi.org/10.1021/acs.est.1c00694

IEA. (2024, February 14). *Trends in batteries – Global EV Outlook 2023 – Analysis - IEA*. https://www.iea.org/reports/global-ev-outlook-2023/trends-in-batteries

Kim, H.-J., Krishna, T. N., Zeb, K., Rajangam, V., Gopi, C. V. V. M., Sambasivam, S., Raghavendra, K. V. G., & Obaidat, I. M. (2020). A Comprehensive Review of Li-Ion Battery Materials and Their Recycling Techniques. *Electronics*, *9*(7), 1161. https://doi.org/10.3390/electronics9071161

Kriston, A., Adanouj, I., Ruiz, V., & Pfrang, A. (2019). Quantification and simulation of thermal decomposition reactions of Li-ion battery materials by simultaneous thermal analysis coupled with gas analysis. *Journal of Power Sources, 435*, 226774. https://doi.org/10.1016/j.jpowsour.2019.226774

Lai, X., Chen, Q., Tang, X., Zhou, Y [Yuanqiang], Gao, F., Guo, Y [Yue], Bhagat, R., & Zheng, Y. (2022). Critical review of life cycle assessment of lithium-ion batteries for electric vehicles: A lifespan perspective. *ETransportation, 12*, 100169. https://doi.org/10.1016/j.etran.2022.100169

Lee, M. (2017). *X-Ray Diffraction for Materials Research: From Fundamentals to Applications* (First edition). Apple Academic Press.

Li, S., & Zhu, J. (2024). Leaching kinetics of fluorine during the aluminum removal from spent Li-ion battery cathode materials. *Journal of Environmental Sciences (China), 138*, 312–325. https://doi.org/10.1016/j.jes.2023.03.017

Liu, J., Shi, H., Hu, X [Xingyu], Geng, Y., Yang, L., Shao, P., & Luo, X. (2022). Critical strategies for recycling process of graphite from spent lithium-ion batteries: A review. *The Science of the Total Environment, 816*, 151621. https://doi.org/10.1016/j.scitotenv.2021.151621

Lombardo, G., Ebin, B., Steenari, B.-M., Alemrajabi, M., Karlsson, I., & Petranikova, M. (2021). Comparison of the effects of incineration, vacuum pyrolysis and dynamic pyrolysis on the composition of NMC-lithium battery cathode-material production scraps and separation of the current collector. *Resources, Conservation and Recycling*, *164*, 105142. https://doi.org/10.1016/j.resconrec.2020.105142

Ma, X., Ge, P., Wang, L [Lisha], Sun, W., Bu, Y., Sun, M., & Yang, Y [Yue] (2023). The Recycling of Spent Lithium-Ion Batteries: Crucial Flotation for the Separation of Cathode and Anode Materials. *Molecules (Basel, Switzerland)*, *28*(10). https://doi.org/10.3390/molecules28104081

Makuza, B., Tian, Q., Guo, X., Chattopadhyay, K., & Yu, D. (2021). Pyrometallurgical options for recycling spent lithium-ion batteries: A comprehensive review. *Journal of Power Sources*, *491*, 229622. https://doi.org/10.1016/j.jpowsour.2021.229622

Malik, M., Chan, K. H., & Azimi, G. (2022). Review on the synthesis of LiNixMnyCo1-x-yO2 (NMC) cathodes for lithium-ion batteries. *Materials Today Energy*, *28*, 101066. https://doi.org/10.1016/j.mtener.2022.101066

Marinescu, I. D. (2000). *Handbook of ceramic grinding and polishing: Properties, processes, technology, tools and typology*. *Materials science and process technology series. Ceramic and other materials--processing and technology*. Noyes Publications [u.a.]. https://www.sciencedirect.com/science/book/9780815513391

Moradi, B., & Botte, G. G. (2016). Recycling of graphite anodes for the next generation of lithium ion batteries. *Journal of Applied Electrochemistry*, *46*(2), 123–148. https://doi.org/10.1007/s10800-015-0914-0

Mousa, E., Hu, X [Xianfeng], Ånnhagen, L., Ye, G., Cornelio, A., Fahimi, A., Bontempi, E., Frontera, P., Badenhorst, C., Santos, A. C., Moreira, K., Guedes, A., & Valentim, B. (2023). Characterization and Thermal Treatment of the Black Mass from Spent Lithium-Ion Batteries. *Sustainability*, *15*(1), 15. https://doi.org/10.3390/su15010015

MWI, Inc. (2023). *Why is graphite used for electrodes?* https://mwi-inc.com/blog-post/why-is-graphite-used-for-electrodes/

Nam, K.-W., Yoon, W.-S., & Yang, X.-Q. (2009). Structural changes and thermal stability of charged LiNi1/3Co1/3Mn1/3O2 cathode material for Li-ion batteries studied by time-resolved XRD. *Journal of Power Sources*, *189*(1), 515–518. https://doi.org/10.1016/j.jpowsour.2008.10.130

O'driscoll, A. (2023). How SEM/EDS Works and Its Applications in Materials Science. *Lab Manager Magazine*. https://www.labmanager.com/how-sem-eds-works-and-its-applications-in-materials-science-30255

Pawlik, M. (2022). Fundamentals of froth flotation. *ChemTexts*, *8*(4), 1–40. https://doi.org/10.1007/s40828-022-00170-5

Ravi Sharma, D P Bisen, Usha Shukla, & B G Sharma. (2012). *X-ray diffraction: a powerful method of characterizing nanomaterials*. https://www.researchgate.net/publication/378107924_X-ray_diffraction_a_powerful_method_of_characterizing_nanomaterials

Rey, I., Vallejo, C., Santiago, G., Iturrondobeitia, M., & Lizundia, E. (2021). Environmental Impacts of Graphite Recycling from Spent Lithium-Ion Batteries Based on Life Cycle Assessment. *ACS Sustainable Chemistry & Engineering*, *9*(43), 14488–14501. https://doi.org/10.1021/acssuschemeng.1c04938

Rinne, T., Klemettinen, A., Klemettinen, L., Ruismäki, R., O'Brien, H., Jokilaakso, A., & Serna-Guerrero, R. (2022). Recovering Value from End-of-Life Batteries by

Integrating Froth Flotation and Pyrometallurgical Copper-Slag Cleaning. *Metals*, *12*(1), 15. https://doi.org/10.3390/met12010015

Ritchie, H., Rosado, P., & Roser, M. (2024). Emissions by sector: where do greenhouse gases come from? *Our World in Data*. https://ourworldindata.org/emissions-by-sector

Ruismäki, R., Rinne, T., Dańczak, A., Taskinen, P., Serna-Guerrero, R., & Jokilaakso, A. (2020). Integrating Flotation and Pyrometallurgy for Recovering Graphite and Valuable Metals from Battery Scrap. *Metals*, *10*(5), 680. https://doi.org/10.3390/met10050680

Stallmeister, C., & Friedrich, B. (2023). Influence of Flow-Gas Composition on Reaction Products of Thermally Treated NMC Battery Black Mass. *Metals*, *13*(5), 923. https://doi.org/10.3390/met13050923

Stone, M. (2021, May 28). As electric vehicles take off, we'll need to recycle their batteries. *National Geographic*. https://www.nationalgeographic.com/environment/article/electric-vehicles-take-off-recycling-ev-batteries

Sun, X., Hao, H., Hartmann, P., Liu, Z., & Zhao, F. (2019). Supply risks of lithium-ion battery materials: An entire supply chain estimation. *Materials Today Energy*, *14*, 100347. https://doi.org/10.1016/j.mtener.2019.100347

Thermo Fischer Scientific. (n.d.–a). *Energy Dispersive X-ray Spectroscopy*. Retrieved August 4, 2024, from https://www.thermofisher.com/de/de/home/materials-science/learning-center/eds-analysis.html

Thermo Fischer Scientific. (n.d.–b). *Principles of Scanning Electron Microscopy*. Retrieved August 4, 2024, from https://www.thermofisher.com/de/de/home/materials-science/learning-center/applications/scanning-electron-microscope-sem-electron-column.html

Thielmann, A., Wietschel, M., Funke, S., Grimm, A., Hettesheimer, T., Langkau, S., Loibl, A., Moll, C., Neef, C., Plötz, P., Sievers, L., Espinoza, L. T., & Edler, J. (2020). *Batterien für Elektroautos: Faktencheck und Handlungsbedarf. Sind Batterien für Elektroautos der Schlüssel für eine nachhaltige Mobilität der Zukunft?* https://ideas.repec.org/p/zbw/fisipp/012020de.html

Thompson, D. L., Hartley, J. M., Lambert, S. M., Shiref, M., Harper, G. D. J., Kendrick, E., Anderson, P., Ryder, K. S., Gaines, L., & Abbott, A. P. (2020). The

importance of design in lithium ion battery recycling – a critical review. *Green Chemistry*, *22*(22), 7585–7603. https://doi.org/10.1039/D0GC02745F

University of Cambridge. (n.d.). *Backscatter imaging*. Retrieved August 4, 2024, from https://caic.bio.cam.ac.uk/electron-microscopy/sem/SEMapplications/backscatter

Vanderbruggen, A. (2022). Lithium-ion batteries recycling with froth flotation – A study on characterization and liberation strategies. *(None)*. https://aaltodoc.aalto.fi/items/b9fd18ba-89df-4c53-a9ec-df8cfb2aec0f

Vanderbruggen, A., Salces, A., Ferreira, A., Rudolph, M., & Serna-Guerrero, R. (2022). Improving Separation Efficiency in End-of-Life Lithium-Ion Batteries Flotation Using Attrition Pre-Treatment. *Minerals*, *12*(1), 72. https://doi.org/10.3390/min12010072

Vanderbruggen, A., Sygusch, J., Rudolph, M., & Serna-Guerrero, R. (2021). A contribution to understanding the flotation behavior of lithium metal oxides and spheroidized graphite for lithium-ion battery recycling. *Colloids and Surfaces a: Physicochemical and Engineering Aspects*, *626*, 127111. https://doi.org/10.1016/j.colsurfa.2021.127111

Vasumathi, N., Sarjekar, A., Chandrayan, H., Chennakesavulu, K., Reddy, G. R., Vijaya Kumar, T. V., El-Gendy, N. S., & Gopalkrishna, S. J. (2023). A Mini Review on Flotation Techniques and Reagents Used in Graphite Beneficiation. *International Journal of Chemical Engineering*, *2023*, 1–15. https://doi.org/10.1155/2023/1007689

Velázquez-Martínez, Valio, Santasalo-Aarnio, Reuter, & Serna-Guerrero (2019). A Critical Review of Lithium-Ion Battery Recycling Processes from a Circular Economy Perspective. *Batteries*, *5*(4), 68. https://doi.org/10.3390/batteries5040068

Wagner-Wenz, R., van Zuilichem, A.-J., Göllner-Völker, L., Berberich, K., Weidenkaff, A., & Schebek, L. (2023). Recycling routes of lithium-ion batteries: A critical review of the development status, the process performance, and life-cycle environmental impacts. *MRS Energy & Sustainability*, *10*(1), 1–34. https://doi.org/10.1557/s43581-022-00053-9

Wang, D., & Liu, Q. (2021). Hydrodynamics of froth flotation and its effects on fine and ultrafine mineral particle flotation: A literature review. *Minerals Engineering*, *173*, 107220. https://doi.org/10.1016/j.mineng.2021.107220

Wen, J., Zhao, D., & Zhang, C. (2020). An overview of electricity powered vehicles: Lithium-ion battery energy storage density and energy conversion efficiency. *Renewable Energy*, *162*, 1629–1648. https://doi.org/10.1016/j.renene.2020.09.055

Windisch-Kern, S., Gerold, E., Nigl, T., Jandric, A., Altendorfer, M., Rutrecht, B., Scherhaufer, S., Raupenstrauch, H., Pomberger, R., Antrekowitsch, H., & Part, F. (2022). Recycling chains for lithium-ion batteries: A critical examination of current challenges, opportunities and process dependencies. *Waste Management (New York, N.Y.)*, *138*, 125–139. https://doi.org/10.1016/j.wasman.2021.11.038

Xie, J., & Lu, Y.-C. (2020). A retrospective on lithium-ion batteries. *Nature Communications*, *11*(1), 2499. https://doi.org/10.1038/s41467-020-16259-9

Yang, H., Zhuang, G. V., & Ross, P. N. (2006). Thermal stability of LiPF6 salt and Li-ion battery electrolytes containing LiPF6. *Journal of Power Sources*, *161*(1), 573–579. https://doi.org/10.1016/j.jpowsour.2006.03.058

Yang, Y [Yue], Huang, G., Xu, S., He, Y [Yinghe], & Liu, X. (2016). Thermal treatment process for the recovery of valuable metals from spent lithium-ion batteries. *Hydrometallurgy*, *165*, 390–396. https://doi.org/10.1016/j.hydromet.2015.09.025

Yang, Z., Huang, H., & Lin, F. (2022). Sustainable Electric Vehicle Batteries for a Sustainable World: Perspectives on Battery Cathodes, Environment, Supply Chain, Manufacturing, Life Cycle, and Policy. *Advanced Energy Materials*, *12*(26), Article 2200383. https://doi.org/10.1002/aenm.202200383

Yu, W., Guo, Y [Yi], Xu, S., Yang, Y [Yue], Zhao, Y., & Zhang, J. (2023). Comprehensive recycling of lithium-ion batteries: Fundamentals, pretreatment, and perspectives. *Energy Storage Materials*, *54*, 172–220. https://doi.org/10.1016/j.ensm.2022.10.033

Zhang, G., Ding, L., Yuan, X., He, Y [Yaqun], Wang, H., & He, J. (2021). Recycling of electrode materials from spent lithium-ion battery by pyrolysis-assisted flotation. *Journal of Environmental Chemical Engineering*, *9*(6), 106777. https://doi.org/10.1016/j.jece.2021.106777

Zhang, G., He, Y [Yaqun], Feng, Y., Wang, H., & Zhu, X. (2018). Pyrolysis-Ultrasonic-Assisted Flotation Technology for Recovering Graphite and LiCoO 2 from Spent Lithium-Ion Batteries. *ACS Sustainable Chemistry & Engineering*, *6*(8), 10896–10904. https://doi.org/10.1021/acssuschemeng.8b02186

Zhang, H., Yang, Y [Yang], Ren, D., Wang, L [Li], & He, X. (2021). Graphite as anode materials: Fundamental mechanism, recent progress and advances. *Energy Storage Materials*, *36*, 147–170. https://doi.org/10.1016/j.ensm.2020.12.027

Supplementary Information 1: Simulated Diffraction Patterns of the Matched Mineralogical Phases

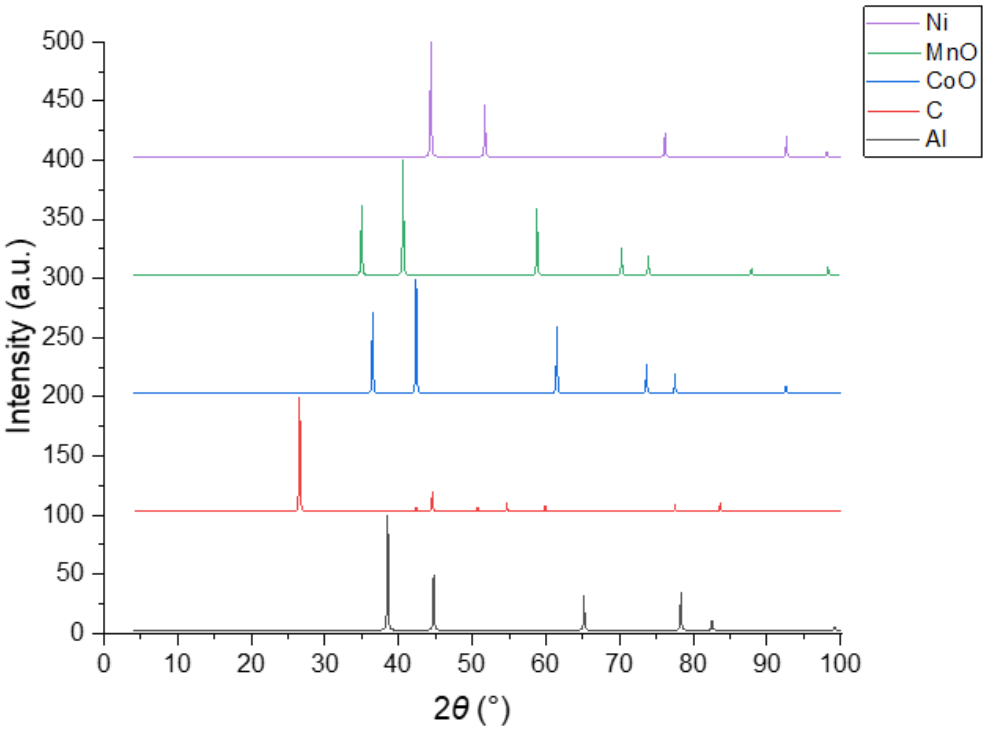

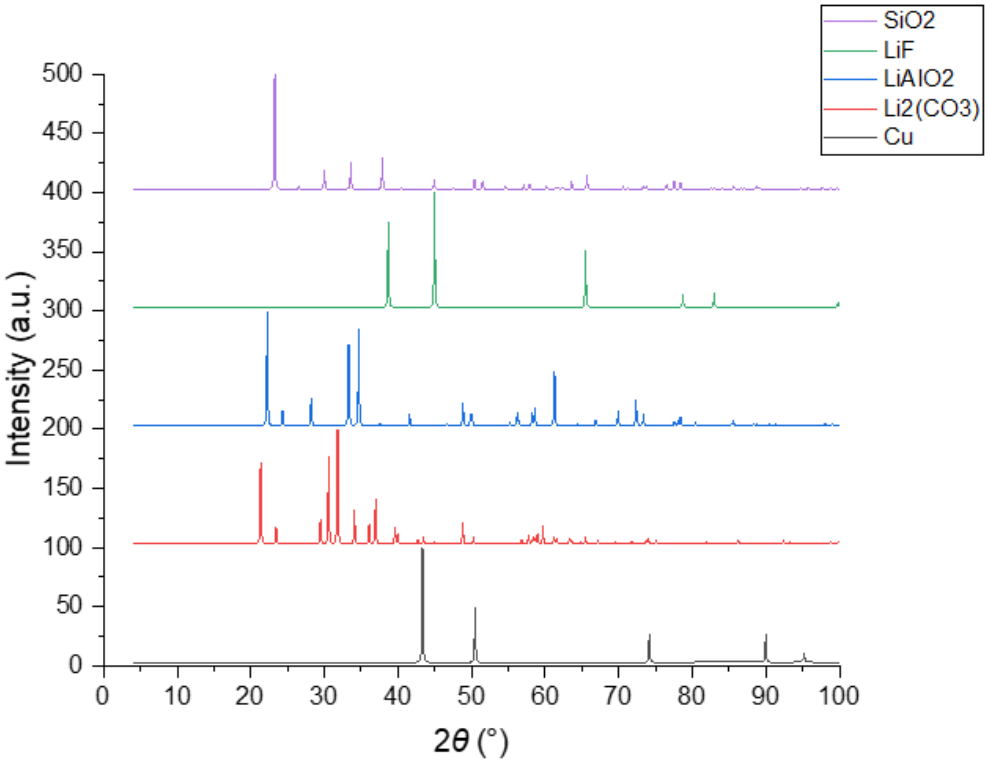

Supplementary Information 2: SEM-EDS mapping

Lettering in the bottom left = [Element] – K_α X-ray emission of the element

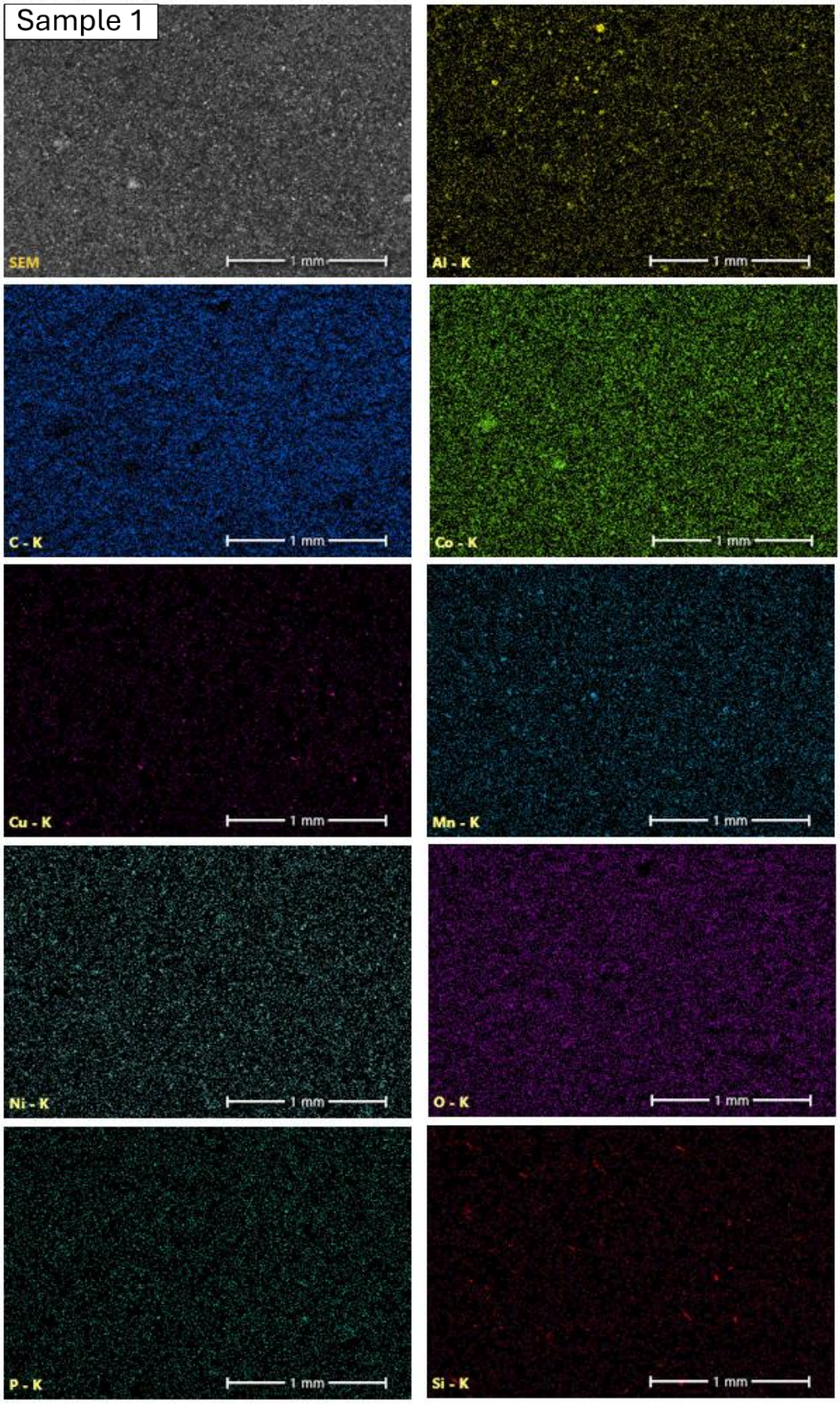

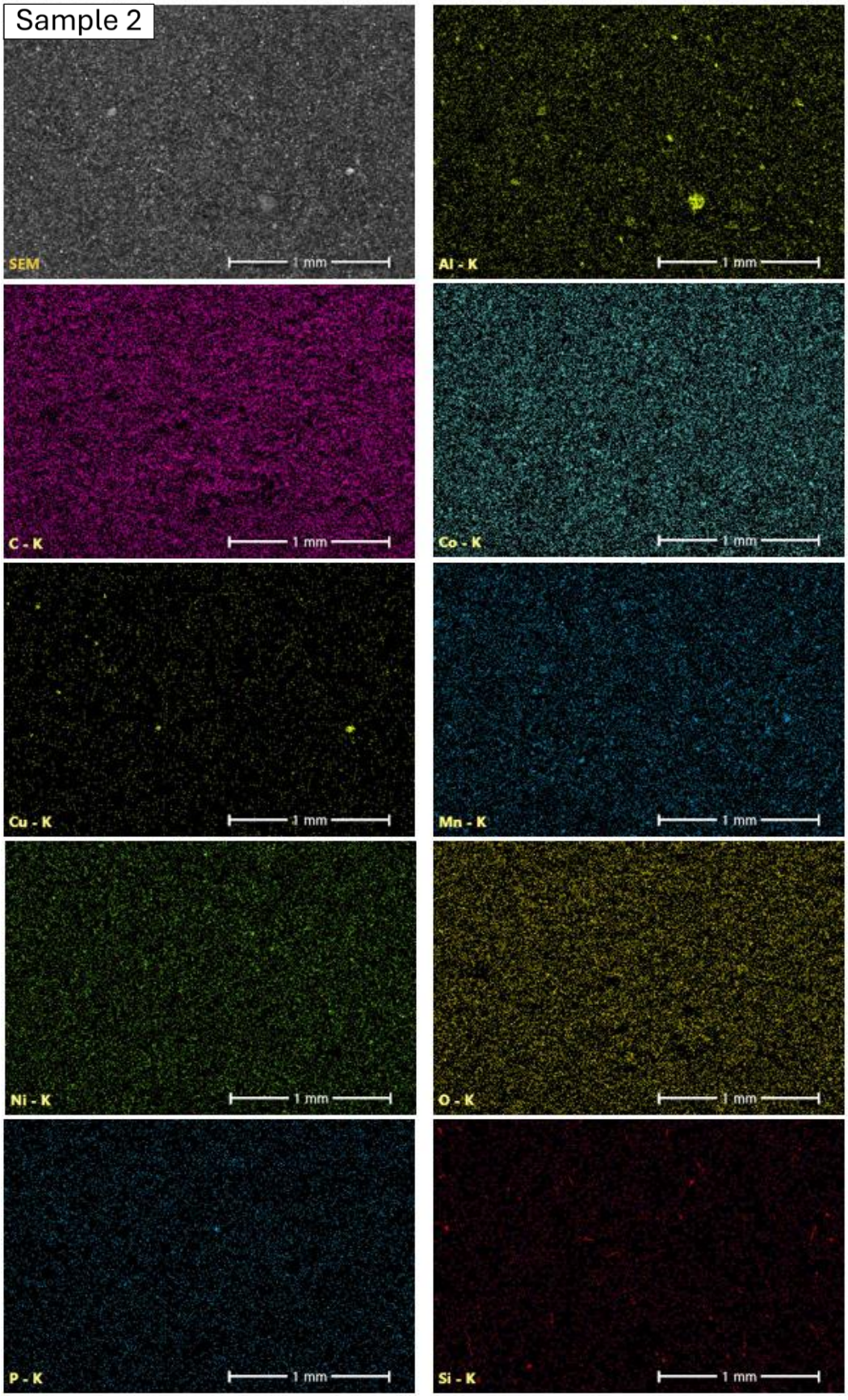
Sample 2
SEM
1 mm
Al - K
1 mm
C - K
1 mm
Co - K
1 mm
Cu - K
1 mm
Mn - K
1 mm
Ni - K
1 mm
O - K
1 mm
P - K
1 mm
Si - K
1 mm

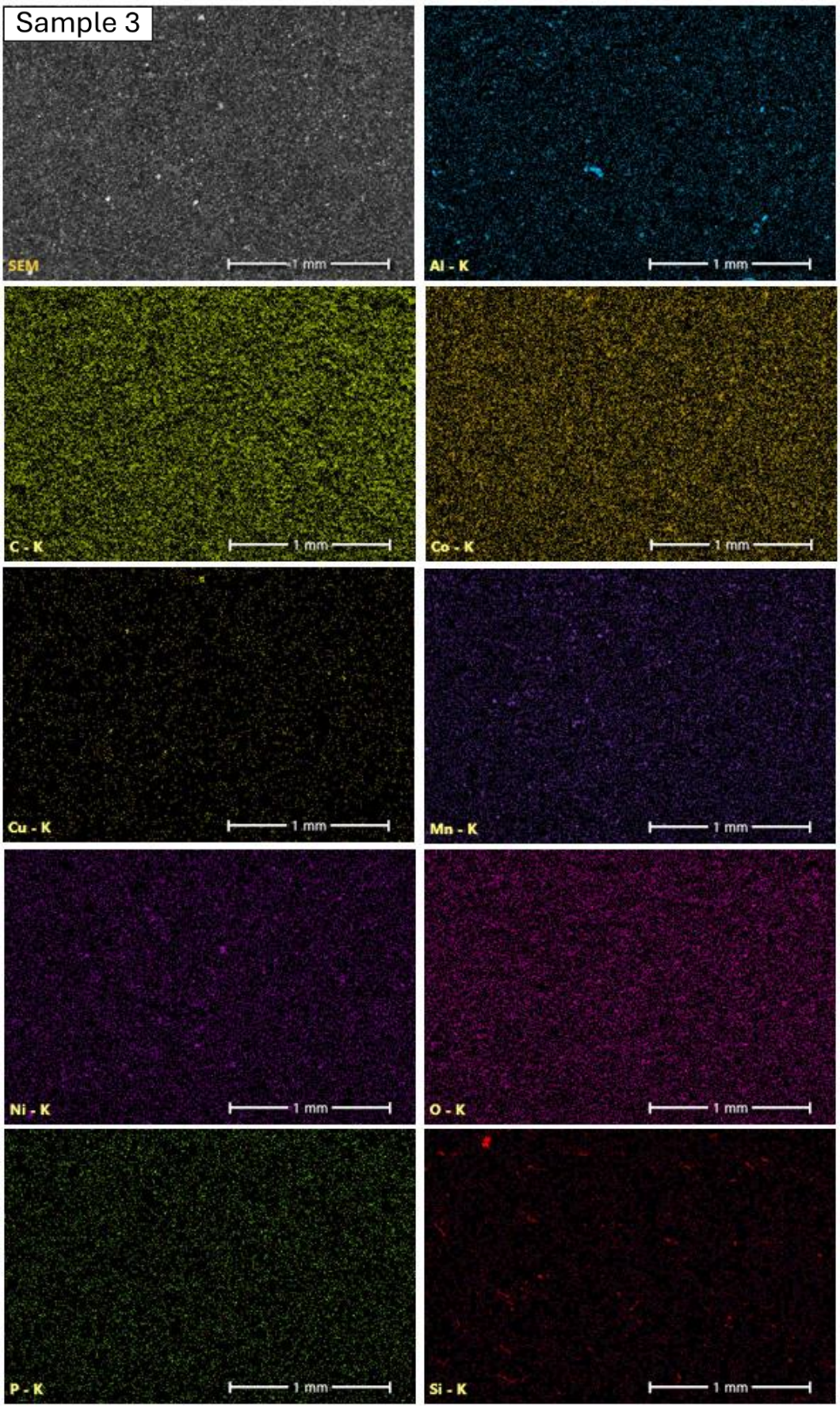
Sample 3
SEM
1 mm
Al - K
1 mm
C - K
1 mm
Co - K
1 mm
Cu - K
1 mm
Mn - K
1 mm
Ni - K
1 mm
O - K
1 mm
P - K
1 mm
Si - K
1 mm

Eidesstattliche Erklärung

Ich versichere, dass ich die vorliegende Arbeit ohne fremde Hilfe und ohne Benutzung anderer als der angegebenen Quellen angefertigt habe, und dass die Arbeit in gleicher oder ähnlicher Form noch keiner anderen Prüfungsbehörde vorgelegen hat. Alle Ausführungen der Arbeit, die wörtlich oder sinngemäß übernommen wurden, sind als solche gekennzeichnet.

[Name, Vorname, Unterschrift (entfällt bei online-Dokumenten)]

[Ort, Datum]

***********Variante für mehrere Autoren* **********

Wir versichern, dass wir die vorliegende Arbeit ohne fremde Hilfe und ohne Benutzung anderer als der angegebenen Quellen angefertigt habe, und dass die Arbeit in gleicher oder ähnlicher Form noch keiner anderen Prüfungsbehörde vorgelegen hat. Alle Ausführungen der Arbeit, die wörtlich oder sinngemäß übernommen wurden, sind als solche gekennzeichnet.

[Name1, Vorname1, Unterschrift1 (entfällt bei online-Dokumenten)]

[Name2, Vorname2, Unterschrift2 (entfällt bei online-Dokumenten)]

[Name3, Vorname3, Unterschrift3 (entfällt bei online-Dokumenten)]

[Name4, Vorname4, Unterschrift4 (entfällt bei online-Dokumenten)]

[Name5, Vorname5, Unterschrift5 (entfällt bei online-Dokumenten)]

[Ort, Datum]